Cell Reports

Article

A senescence restriction point acting on chromatin integrates oncogenic signals

Graphical abstract

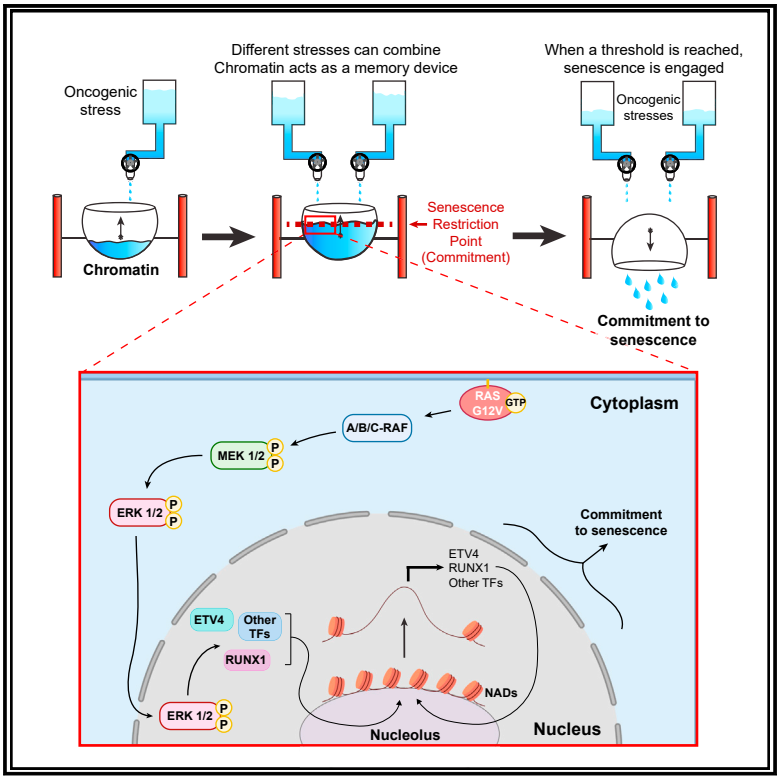

Highlights

- Senescence restriction point integrates stress signals through non-coding chromatin opening
- Chromatin opening acts as a memory print of oncogenic threats to trigger senescence
- ERK2 mediates chromatin opening through a network of TFs, including ETV4 and RUNX1
- ETV4 and RUNX1 are high in human benign lesions of the pancreas and lost in PDAC

Authors

Stéphane Lopes-Paciencia, Véronique Bourdeau, Marie-Camille Rowell, ..., Simon Turcotte, Adrian Serohijos, Gerardo Ferbeyre

Correspondence

g.ferbeyre@umontreal.ca

In brief

Cellular stress sensors are vital for health and homeostasis. Lopes-Paciencia et al. show that chromatin acts as an oncogenic stress sensor, controlling the decision between cell proliferation and senescence. Oncogenic signals trigger transcription factors, which open chromatin and commit cells to senescence, a commitment that persists even after the initial stress subsides.

Lopes-Paciencia et al., 2024, Cell Reports *43*, 114044
April 23, 2024 Crown Copyright © 2024 Published by Elsevier Inc.
https://doi.org/10.1016/j.celrep.2024.114044

CellPress

Cell Reports

CellPress
OPEN ACCESS

Article

A senescence restriction point acting on chromatin integrates oncogenic signals

Stéphane Lopes-Paciencia,[1] Véronique Bourdeau,[2,6] Marie-Camille Rowell,[1,6] Davoud Amirimehr,[2] Jordan Guillon,[1] Paloma Kalegari,[1] Arnab Barua,[2] Vincent Quoc-Huy Trinh,[1,3,4] Feryel Azzi,[1] Simon Turcotte,[1,5] Adrian Serohijos,[2] and Gerardo Ferbeyre[1,2,7,*]

[1]Centre de recherche du Centre Hospitalier de l'Université de Montréal (CRCHUM), Montréal, QC H2X 0A9, Canada
[2]Département de Biochimie et Médecine Moléculaire, Université de Montréal, Montréal, QC H3C 3J7, Canada
[3]Institut de recherche en immunologie et en cancérologie (IRIC), Université de Montréal, Montréal, QC H3C 3J7, Canada
[4]Département de pathologie, Centre hospitalier de l'Université de Montréal, Montréal, QC, Canada
[5]Département de chirurgie, Service de chirurgie hépatopancréatobiliaire, Centre hospitalier de l'Université de Montréal, Montréal, QC, Canada
[6]These authors contributed equally
[7]Lead contact
*Correspondence: g.ferbeyre@umontreal.ca
https://doi.org/10.1016/j.celrep.2024.114044

SUMMARY

We identify a senescence restriction point (SeRP) as a critical event for cells to commit to senescence. The SeRP integrates the intensity and duration of oncogenic stress, keeps a memory of previous stresses, and combines oncogenic signals acting on different pathways by modulating chromatin accessibility. Chromatin regions opened upon commitment to senescence are enriched in nucleolar-associated domains, which are gene-poor regions enriched in repeated sequences. Once committed to senescence, cells no longer depend on the initial stress signal and exhibit a characteristic transcriptome regulated by a transcription factor network that includes ETV4, RUNX1, OCT1, and MAFB. Consistent with a tumor suppressor role for this network, the levels of ETV4 and RUNX1 are very high in benign lesions of the pancreas but decrease dramatically in pancreatic ductal adenocarcinomas. The discovery of senescence commitment and its chromatin-linked regulation suggests potential strategies for reinstating tumor suppression in human cancers.

INTRODUCTION

Cell number regulation hinges on cell fate determinations, encompassing proliferation, quiescence, cell death, and senescence. These processes are vital for normal development, adult physiology, and conditions characterized by abnormal cell proliferation, such as cancer, or the buildup of senescent cells, as observed in aging. Numerous extracellular factors influence cell fate by modulating mitogenic pathways, notably the RAS-MAPK pathway. The decision between proliferation and quiescence is believed to be controlled by a pivotal juncture known as the restriction point (R). Beyond this point, cells no longer rely on mitogens for proliferation because an intrinsic mitogenic signal propels them into the proliferative phase.[1] The molecular mechanism that explains the actions at the restriction point involves the activation of the cyclin-dependent kinases that inhibit the retinoblastoma protein, leading to the expression of proliferation genes mediated to a large extent by the E2F transcription factor (TF) family.[2]

The activation of the ERK pathway can lead to proliferation, senescence, cell death, or differentiation. However, little is known about the mechanisms that regulate these different cell fate decisions. Previous work established that moderate ERK signaling stimulates proliferation, whereas excessive signaling triggers senescence.[3,4] Here, we took advantage of the conditional activation of oncogenic RAS to discover that the proliferation-senescence decision is controlled by a senescence restriction point (SeRP) beyond which RAS-ERK signals are no longer required to enter senescence. At the molecular level, sustained and high ERK signaling engages a TF network that leads to chromatin opening and the expression of proinflammatory genes. This chromatin opening seems to act as a memory print of oncogenic stresses that facilitates the triggering of oncogene-induced senescence (OIS). Consistent with a key role for TFs in mediating senescence commitment, inactivation of certain TFs identified in this study reverted senescence-associated gene expression changes, whereas their overexpression was sufficient to drive senescence. Two of these TFs, ETV4 and RUNX1, were highly expressed in benign lesions of the pancreas, which contain senescent cells[5,6,] and were downregulated in pancreatic adenocarcinomas. This suggests that the SeRP could be important for the tumor suppressor program occurring in early pancreatic carcinogenesis *in vivo*. We thus propose that

This is an open access article under the CC BY license (http://creativecommons.org/licenses/by/4.0/).

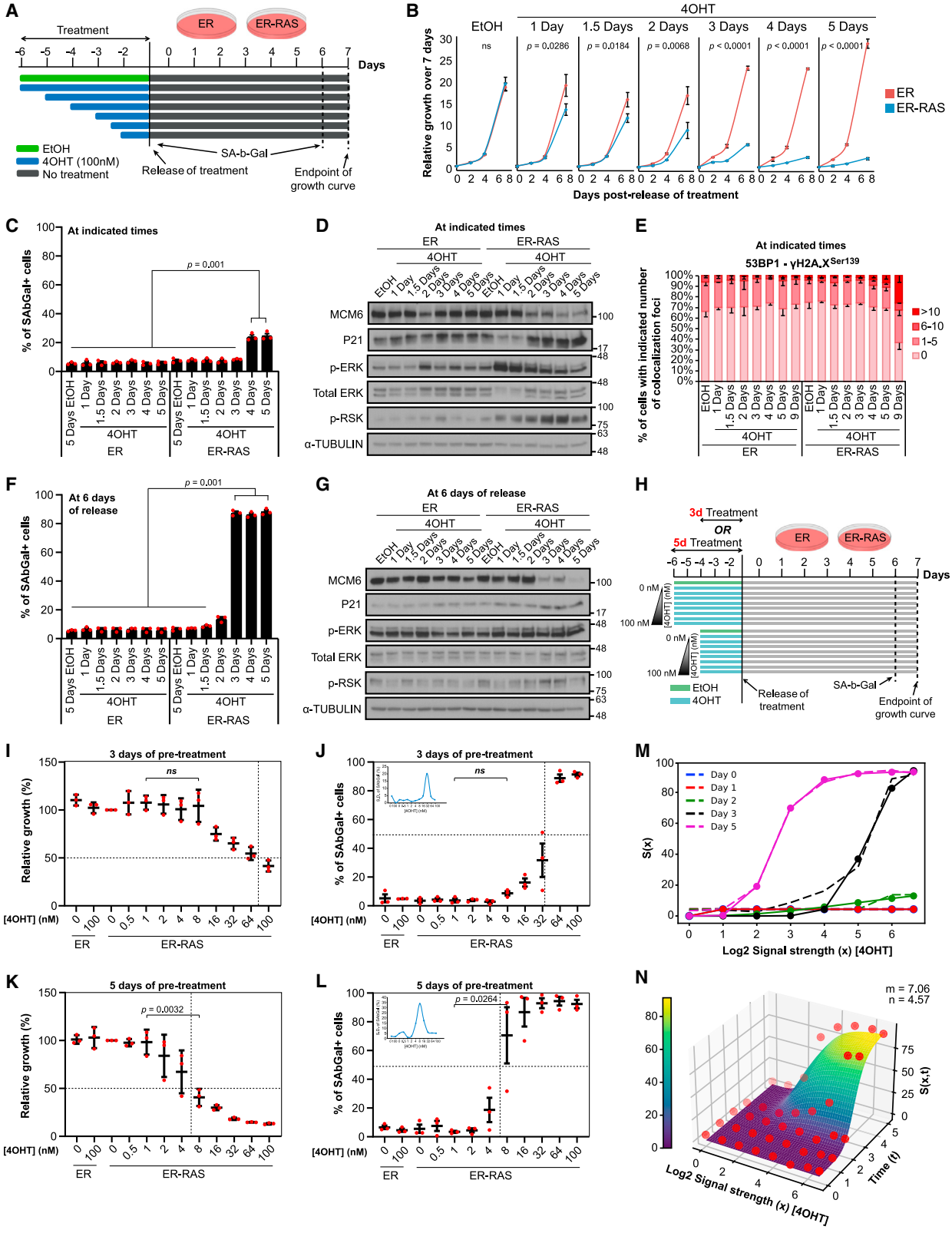

(legend on next page)

senescence is an epigenetically controlled response that integrates signals from different oncogenes by increasing chromatin accessibility mostly in gene-poor regions of the genome.

RESULTS

The senescence restriction point (SeRP) depends on the duration and intensity of oncogenic signaling

To investigate how ERK signaling dynamics controls the entry into senescence, we expressed the ligand-binding domain of the estrogen receptor (ER) alone or fused to an oncogenic allele (G12V) of HRAS (ER-RAS) in normal human diploid fibroblasts (NHDFs) IMR90. The ER-RAS allele renders RAS-MAPK signaling conditional to treatment with 4-hydroxytamoxifen (4OHT), allowing the modulation of signaling intensity and duration. We first varied the time of ERK stimulation to determine how long ERK signaling is required to commit cells to senescence (Figure 1A). We found that stimulation of RAS-MAPK signaling with 4OHT for $\geq$3 days engaged the cells to a stable proliferation arrest, whereas shorter stimulation did not (Figure 1B). Of note, after 3 days of stimulation, cells were negative for senescence-associated β-galactosidase (SA-β-Gal) staining (Figure 1C), had a moderate induction of p21, a slight reduction of the E2F target MCM6 (Figure 1D), and had no increase in DNA damage response (Figure 1E). However, cells induced for $\geq$3 days were SA-β-Gal$^+$ 6 days after ending ERK stimulation, whereas cells induced for 1, 1.5, or 2 days were not (Figure 1F). These cells also had a strong induction of p21 and reduction of MCM6 (Figure 1G), indicating that they are fully senescent. Together, these results define a time window in which cells are still negative for senescence markers but already engaged toward senescence. Similar results were reproduced in MRC5, another NHDF cell line (Figure S1).

In addition to duration, signaling strength can control cell fate after ERK stimulation.[7,8] To investigate the interplay between signaling duration and intensity, we varied ERK signaling strength in the ER-RAS system using different concentrations of 4OHT. As a control, we validated that pERK levels were finely tuned by different 4OHT concentrations at the single-cell level (Figure S2A). We found that commitment to senescence required concentrations >32 nM of 4OHT for 3 days (Figures 1H–1J). However, upon a longer time of stimulation, weaker signals also induced senescence (Figures 1K–1L). Therefore, cells integrate both the duration and intensity of ERK signaling to commit to cellular senescence (Figures 1M and 1N). The dynamics of commitment as a function of the duration and amplitude of the initial input fits a model of a bistable system controlled by both signaling intensity (Hill coefficient n = 4.57) and signaling time (Hill coefficient m = 7.06) (Figure 1N). Bistable switch-like responses were previously described for ERK-mediated maturation in frog oocytes[9] and imply that the system becomes ultrasensitive to small changes in the regulatory signal when a certain threshold is attained. A hallmark of this behavior is an increase in the variance during the transition point between the two states,[10] as seen in the inserts of Figures 1J and 1L.

To confirm the essential role of ERK kinases during the commitment to senescence, we used the ERK inhibitor SCH772984 or the MEK inhibitor AZD6244. As expected, both drugs prevented the senescence commitment to ER-RAS activation when cotreated with 4OHT for 3 days (Figures S2B–S2E). However, cells committed to senescence after 3–4 days of ERK activation remained committed even if ERK signaling was brought back to basal levels using the inhibitors (Figures S2F–S2I). Thus, we concluded that oncogenic ERK

Figure 1. Commitment to RAS-induced senescence integrates duration and intensity of ERK signaling

(A) Schedules for activation and inactivation of ERK in the ER-RAS system.

(B) Representative growth curves of IMR90 cells infected with ER or ER-RAS, pretreated with vehicle (EtOH) or 100 nM 4OHT for the indicated time and then released (N= 4). Error bars represent SD. An unpaired t test with a 2-tailed p value is indicated for each treatment, comparing ER (control) to ER-RAS.

(C) Percentage of SA-β-Gal$^+$ cells at indicated time points of treatment for ER and ER-RAS-infected cells. N = 3, with the mean of each biological replicate indicated by a dot. Error bars represent SD. One-way ANOVA with Dunnett's correction, followed by Tukey's honest significant difference (Tukey-HSD) were performed. At least 3 × 100 cells were counted per condition per biological replicate.

(D) Representative western blot analysis of cells as in (C) at indicated times of treatment (N = 3).

(E) Quantification of DNA damage foci represented by colocalization of 53BP1 and γH2A.X Ser139 by immunofluorescence performed on cells as in (C). Mean of 2 biological replicates is shown with SD as error bars; ±200 cells counted per condition (N= 2).

(F) Percentage of SA-β-Gal$^+$ cells in cells pretreated for the indicated time and then released for 6 days, N = 3, with each replicate value indicated as a red dot. Error bars represent SD. One-way ANOVA with Dunnett's correction, followed by Tukey-HSD were performed. At least 3 × 100 cells are counted per condition per biological replicate.

(G) Representative western blot as in (D) but 6 days posttreatment release (N = 3).

(H) Schematic representation of 4OHT treatments for the identification of the senescence-engaging threshold point dependent on the intensity of ERK signaling.

(I) Percentage of relative growth after 7 days of ER and ER-RAS cells pretreated for 3 days with a gradient of 4OHT. N = 3, with the mean of each biological replicate indicated by a dot. Error bars represent SD.

(J) Percentage of SA-β-Gal$^+$ cells 6 days postrelease of treatment, in cells from (I) pretreated for 3 days with a gradient of 4OHT. N = 3, with the mean of each biological replicate indicated by a red dot. Error bars represent SEM. The inset shows the increased variance in percentage of SA-β-Gal at the commitment restriction point as depicted by the bell curve.

(K) Same as in (I) but with cells pretreated for 5 days.

(L) Same as in (J) but with cells pretreated for 5 days. For (I)–(L), the p value was calculated by performing an unpaired t test between 1- and 8-nM conditions in ER-RAS-expressing cells.

(M) A 2-dimensional Hill function (solid line with dots) is fitted to the experimental data (dashed line) from (C), (F), (K), and (L). The sigmoidal Hill function shows the on-off mechanism of this bistable system at ~3 days of 4OHT.

(N) A 3-dimensional Hill function is fitted to the data from (C), (F), (K), and (L). Equation fit and parameters of the Hill function are calculated using Python's curve_fit function. Passage through the SeRP represents a bistable mechanism.

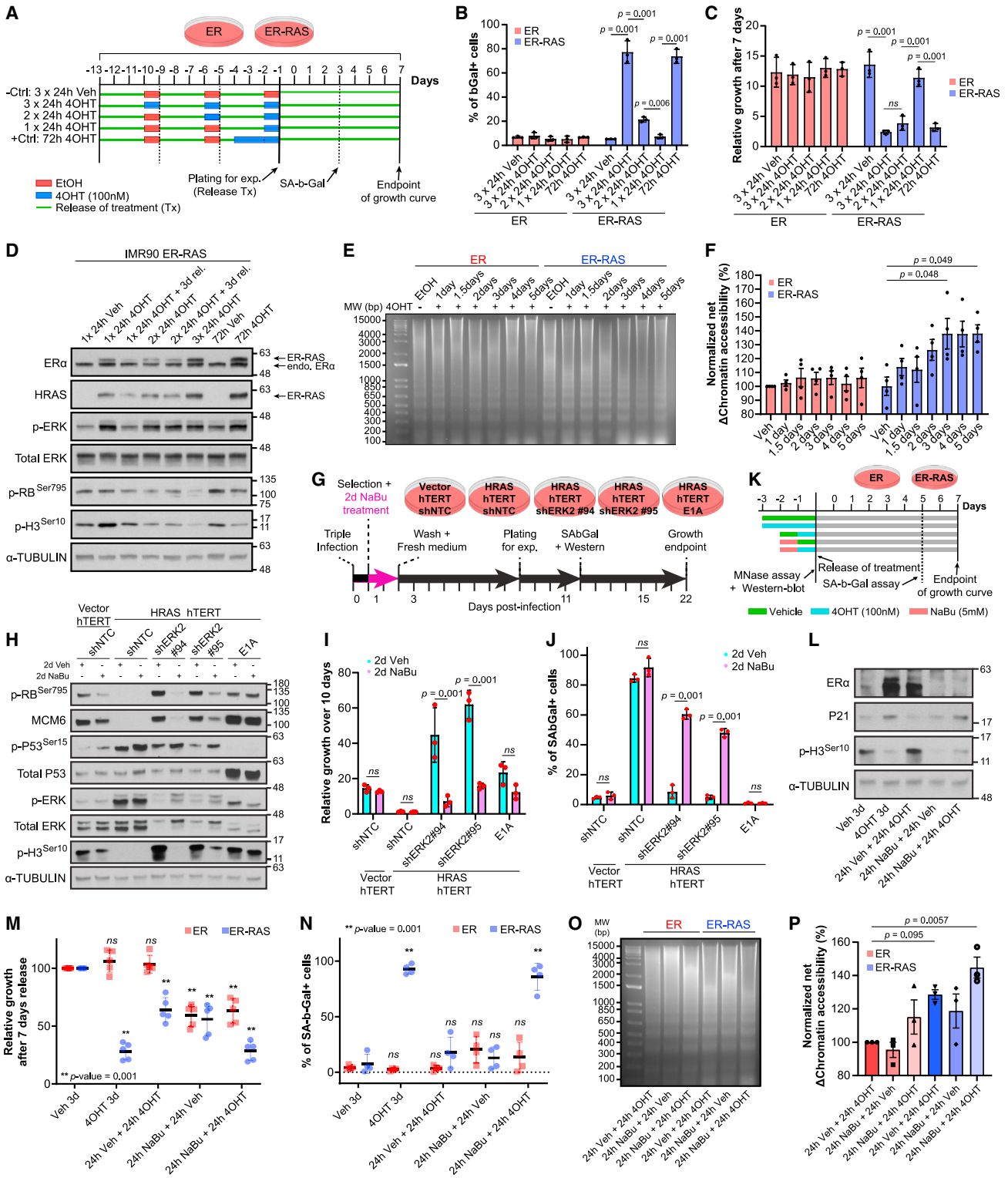

Figure 2. Commitment to RAS-induced senescence is integrated at the chromatin level by ERK2 kinases

(A) Schematic representation of the experiment performed in (B) and (C). IMR90 cells expressing either ER or ER-RAS were treated with 100 nM 4OHT by pulses of 24 h, each separated by 3 days.

(B) Percentage of SA-β-Gal^{+} cells for cells described in (A). N = 3, with the mean of each biological replicate indicated by a dot. Error bars represent SD. One-way ANOVA with Dunnett's correction, followed by Tukey-HSD were performed.

(legend continued on next page)

signaling needs to be maintained long enough to trigger the senescence commitment checkpoint beyond which ERK activation is no longer essential to induce senescence. Together, these results define an SeRP that can help to distinguish between signals that are physiological and transient from those potentially procancer coming from mutant oncoproteins.

Memory and integration of aberrant signaling

Bistable systems respond to stimuli depending on their history, a phenomenon known as hysteresis.[11] For this reason, we next investigated whether cells retain a trace of aberrantly high RAS-MAPK activation. We induced ER-RAS in short pulses of 24 h separated by 3 days of release that included replating the cells. Commitment to senescence was induced by 3 days of consecutive RAS activation as before or by 3 days of cumulative RAS activation (3 pulses of 24 h), but not by 2 pulses of 24 h, indicating that cells remember aberrant ERK signaling for several days after the initial stimulation (Figures 2A–2C). We confirmed that both the expression of the ER-RAS transgene and the levels of phospho-ERK (p-ERK) were almost completely renormalized upon 3 days of release and replating of cells (Figure 2D), validating that the observed results were not a result of continued ERK signaling. A memory of aberrant signaling is important to trigger senescence because the molecular trace of aberrant signaling could provide an opportunity to integrate different oncogenic signals.

To investigate whether aberrant ERK signaling combines with additional oncogenic stimuli to induce senescence, we activated ERK using ER-RAS in MYC-expressing cells (Figure S3A). As before, 3 days of RAS activation triggered growth arrest and senescence in control cells that do not express MYC. However, activating ER-RAS for only 1 or 2 days in MYC-expressing cells also induced a lasting growth arrest accompanied by a characteristic hypertrophic morphology of senescent cells, an increase in p21, a decrease in phospho-H3 levels and Ki67, and an increase in inflammatory cytokine expression (Figures S3B–S3I). Furthermore, activating ERK with 4OHT triggered sensitivity to the senolytic agent ABT-263 in MYC-expressing cells, whereas ER-RAS vector cells even after 3 days of 4OHT treatment were not sensitive to this agent (Figure S3B). This confirms that ERK and MYC signaling cooperate to trigger senescence. Intriguingly, RAS and MYC cooperation for senescence induction was not dependent on an increased intensity of ERK activation (Figure S3C). Instead, MYC overexpression importantly reduced basal ERK signaling. This result highly suggests that the integration of oncogenic signals occurs downstream of ERK, most probably at the chromatin level where both MYC and ERK signals converge.[12,13]

To investigate the overall chromatin conformation at senescence commitment, we first used MNase assays. We found a sudden increase in chromatin opening just before the time of commitment (Figures 2E and 2F). We previously showed that inactivating ERK2 bypassed RAS-induced senescence, allowing malignant transformation.[3] Interestingly, the addition of the histone deacetylase (HDAC) inhibitor sodium butyrate (NaBu) during the transformation of primary cells by RAS activation and ERK depletion (shERK2) (Figure 2G) restored senescence and inhibited transformation (Figures 2H–2J). NaBu alone did not induce senescence in control vector cells or in cells transformed by E1A and RAS, and therefore is not acting as a non-specific senescence inducer. Thus, we concluded that the tumor suppressor role of ERK2 in RAS-induced senescence depends, at least in part, on its ability to mediate chromatin opening. In other words, chromatin opening can substitute for excessive ERK signals to suppress RAS-dependent transformation. In agreement with this idea, treating cells with NaBu shortened the commitment window of ER-RAS cells (Figures 2K–2N) from 3 days to 1 day of signaling without increasing the expression of the transgene (Figure 2L). Moreover, this was associated with an earlier opening of the chromatin (Figures 2O and 2P). This suggested

(C) Relative growth over 7 days of cells described in (A). N = 3, with the mean of each biological replicate indicated by a dot. Error bars represent SD. One-way ANOVA with Dunnett's correction, followed by Tukey-HSD were performed.
(D) Representative western blot performed on whole-cell lysates from cells depicted in (A); N = 3.
(E) Representative MNase assay was performed on IMR90 cells expressing ER or ER-RAS and treated with vehicle or 100 nM 4OHT for indicated times; N= 3.
(F) Quantification of MNase assays performed in (E) indicating the net percentage of chromatin opening. N = 4, with each biological value represented as a black dot. Error bars represent SEM. One-way ANOVA with Dunnett's correction, followed by Tukey-HSD were performed.
(G) Schematic representation of experiments for (H)–(J). IMR90 cells infected with hTERT and vector or HRAS and shNTC or shERK2 (nos. 94 or 95) were treated for 2 days with 5 mM NaBu starting at day 1 postinfection.
(H) Representative western blot, performed on whole-cell lysates from cells depicted in (G); N = 2.
(I) Relative growth over 10 days of cells from (G). N = 3, with the mean of each biological replicate indicated by a dot. Error bars represent SD. One-way ANOVA with Dunnett's correction, followed by Tukey-HSD were performed.
(J) Percentage of SA-β-Gal$^+$ cells in cells depicted in (G). N = 3, with the mean of each biological replicate indicated by a dot. Error bars represent SD. One-way ANOVA with Dunnett's correction, followed by Tukey-HSD were performed.
(K) Schematic representation of experiments in (L)–(P). IMR90 cells expressing either ER or ER-RAS were treated for 24 h with 5 mM of HDAC inhibitor NaBu followed or not by 24 h of 100 nM 4OHT to assess the possibility of shifting the SeRP window.
(L) Representative western blot performed on whole-cell lysates from cells depicted in (K); N = 2.
(M) Percentage of relative growth after 7 days of release of cells from (K). N = 5, with the mean of each biological replicate represented as a dot. Error bars represent SD. One-way ANOVA with Dunnett's correction, followed by Tukey-HSD were performed, comparing vehicle 3-day condition to all of the other treatment regimens within ER or ER-RAS conditions.
(N) Percentage of SA-β-Gal$^+$ cells for cells depicted in (K). N = 3, with the mean of each biological replicate indicated by a dot. Error bars represent SD. One-way ANOVA with Dunnett's correction, followed by Tukey-HSD were performed, comparing vehicle 3-day condition to all of the other treatment regimens within ER or ER-RAS conditions.
(O) Representative MNase assay performed on cells shown in (K); N = 3.
(P) Quantification of MNase assays performed in (O) indicating the net percentage of chromatin opening. N = 3, with each biological value represented as a dot. Error bars represent SEM. One-way ANOVA with Dunnett's correction, followed by Tukey-HSD were performed.

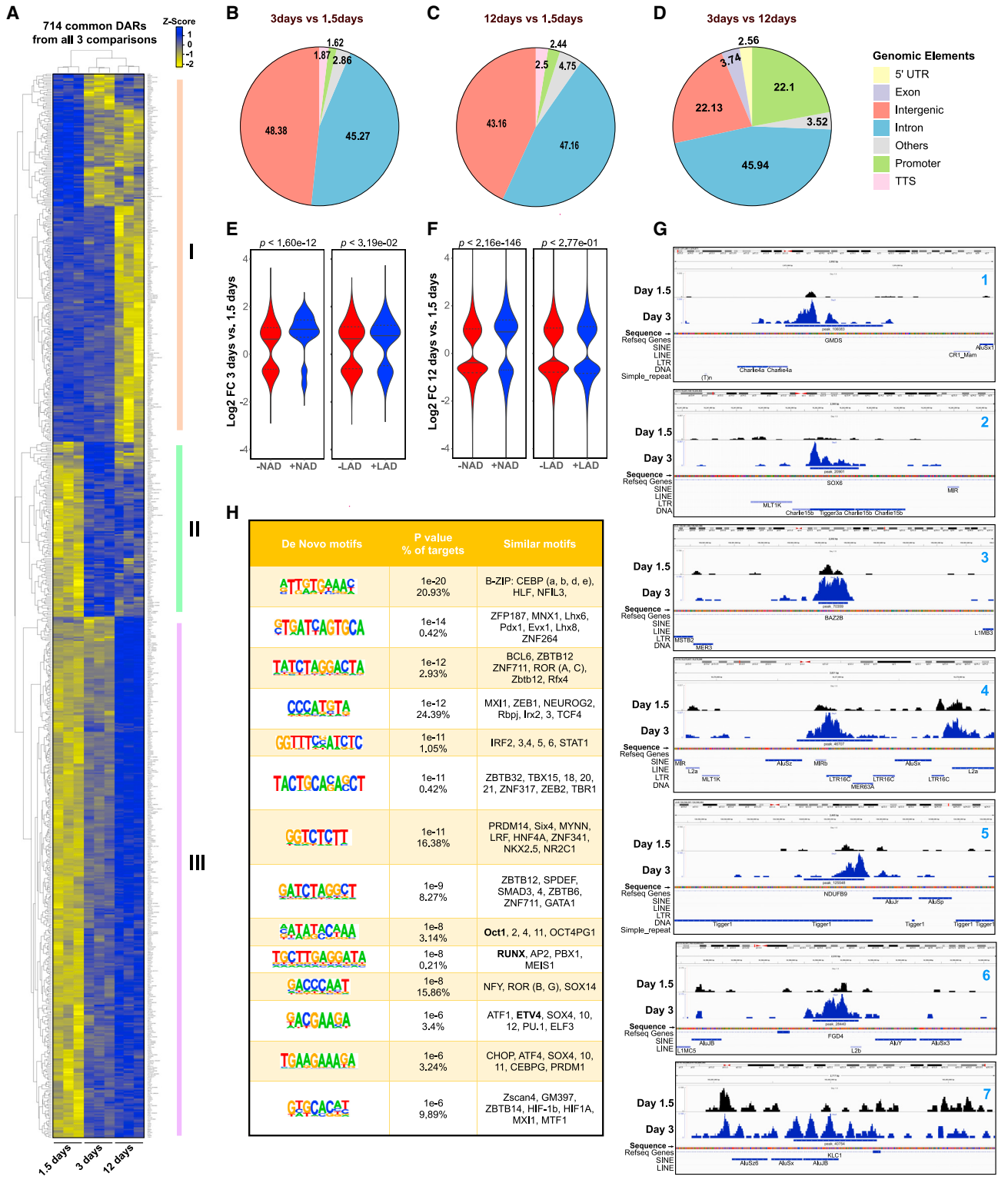

Figure 3. ATAC-seq analysis of senescence commitment

(A) Heatmap showing DARs common to cells expressing ER-RAS for 1.5 days (uncommitted), 3 days (committed), and 12 days (senescent); N = 3.
(B–D) Pie charts for genome-wide distribution of DARs.

(legend continued on next page)

an active role for chromatin opening in mediating commitment to senescence.

To further support a role for chromatin opening in the commitment at the SeRP, we looked at the chromatin both in cells where commitment changes as a function of ERK activation by different concentrations of 4OHT and in cells that committed to senescence earlier due to the combined expression of MYC and RAS. We found that to attain the levels of chromatin opening we obtained after treatment with a high concentration of 4OHT for 3 days (Figures 2E and 2F), low concentrations of 4OHT required 5 days of treatment (Figures S2J and S2K). In addition, we found that cells expressing both RAS and MYC have more open chromatin than cells expressing each oncogene alone (Figures S3J and S3K).

The cooperation between RAS and MYC to open chromatin and induce senescence seems to contrast with early studies in murine fibroblasts that showed that these oncogenes cooperate to transform primary cells.[14] However, this cooperation was later shown to be dependent on p53 inactivation to avoid Myc-induced apoptosis.[15] To further clarify this point, we interrogated 90,354 samples from 87,240 cancer patients in the cBioPortal for KRAS and MYC mutations. The data show that KRAS and MYC alterations (mutations and amplifications) preferentially exclude one another as is expected by signals that cooperate to trigger a senescence tumor suppressor response (Figure S3L). Taken together, the data suggest that commitment to senescence is mediated by chromatin opening, which acts as a mechanism to integrate both the intensity and the duration of oncogenic signals (Figure S3M).

The chromatin of repeated sequences and nucleolar-associated domains (NADs) gains accessibility upon commitment to senescence

Having identified the chromatin opening associated with the commitment to RAS-induced senescence, we went on to identify which genomic regions were targeted by this mechanism. Thus, we performed the assay for transposase-accessible chromatin with sequencing (ATAC-seq) to identify the differentially accessible regions (DARs) between uncommitted cells (day 1.5), committed cells (day 3), and already-senescent cells (day 12). Principal-component analysis (PCA) analysis clearly showed that each of these stages has distinctive patterns of chromatin exposition (Figure S4A). A heatmap including 714 common DARs (open and closed) showed 3 clusters (I–III) representing regions open in uncommitted, committed, and senescent cells, respectively. Interestingly, committed cells display open peaks across most of these clusters (Figure 3A). Moreover, a heatmap focusing on all 1,533 unique open DARs shows that committed cells have many open peaks in common with both senescence and uncommitted cells, which is consistent with a wider distribution of exposed chromatin during commitment (Figure S4B). Interestingly, the regions open on day 1.5 were also open on day 3 and were closed on day 12. Also, the regions open on day 12 were closed on day 1.5, but many of them were also open on day 3 (Figure S4B). These results suggest that committed cells are in a transition state of chromatin rearrangement between uncommitted and senescent cells.

Gene Ontology analysis using g-profiler and hypergeometric optimization of motif enrichment (HOMER) indicates that closed DARs in senescent cells in comparison with uncommitted cells were near many genes in ALK and RHO signaling pathways (Figure S4C). Also, closed peaks were associated with the cell cycle (logP −55.5) and mitosis (logP −51.4), and open peaks were associated with axon guidance (logP −29.6) and growth factor signaling (i.e., vascular endothelial growth factor, logP −17.48). Closed DARs in committed cells in comparison with uncommitted cells revealed significant enrichment near genes for Robo signaling (logP −10.7) and cell junction (logP −10.01). Regions that were specifically open due to commitments relative to uncommitted cells were closed to genes controlling collagen degradation (logP −13.18). Volcano plots for the comparisons between day 3 vs. day 1.5 and day 12 vs. day 1.5 summarize the top genes near open or closed DARs. Note that committed cells have much more open regions than closed regions, which indicates again a more accessible chromatin (Figures S4D and S4E).

Genome ontology analysis of open DARs between committed and uncommitted cells revealed that most of them mapped to intergenic regions and introns (Figures 3B and 3C). A similar observation was made for senescent vs. uncommitted cells explaining the modest match of ATAC-seq peaks with classic senescence signatures. However, DARs open in committed cells relative to senescent cells were differently distributed and included a higher proportion of gene promoters (Figure 3D), reflecting the fact that committed cells are still proliferating and express cell-cycle genes. Studies on chromatin accessibility during replicative senescence concluded that gene-poor NADs and lamin-associated domains (LADs) were largely responsible for more open chromatin in senescent cells.[16] In line with this investigation, peaks that coincided with NADs and LADs in committed cells exhibited higher openness compared to uncommitted cells. Excluding peaks associated with NADs or LADs eliminated the differences between these cell stages (Figure 3E). Similarly, when comparing senescent cells (day 12) to uncommitted cells (day 1.5), peaks excluded from NADs and LADs showed a decreased level of openness compared to peaks overlapping with NADs and LADs (Figure 3F). Several examples of commitment-specific peaks are shown in Figure 3G displaying their

(E) Violin plots of average log2fold change (FC) distribution of open regions between day 3 and day 1.5 for all ATAC-seq peaks that are excluded (red) or overlap (blue) with NADs (left) or LADs (right). The Wilcoxon rank-sum test was used to compare the distributions of log2FC values between day 3 and day 1.5.
(F) As in (E) but comparing open regions between day 12 and day 1.5.
(G) Integrative Genomics Browser snapshot depicting representative ATAC-seq signals in committed cells in comparison with uncommitted cells showing the location of different families of repeated sequences.
(H) HOMER *de novo* motif analysis of open peaks at day 3 in comparison with day 1.5. Motif enrichment was calculated with HOMER software using the cumulative binomial distribution adjusted for multiple testing with the Benjamini-Hochberg method. The total target of sequences used was 1,911 and the total background of sequences was 140,529.

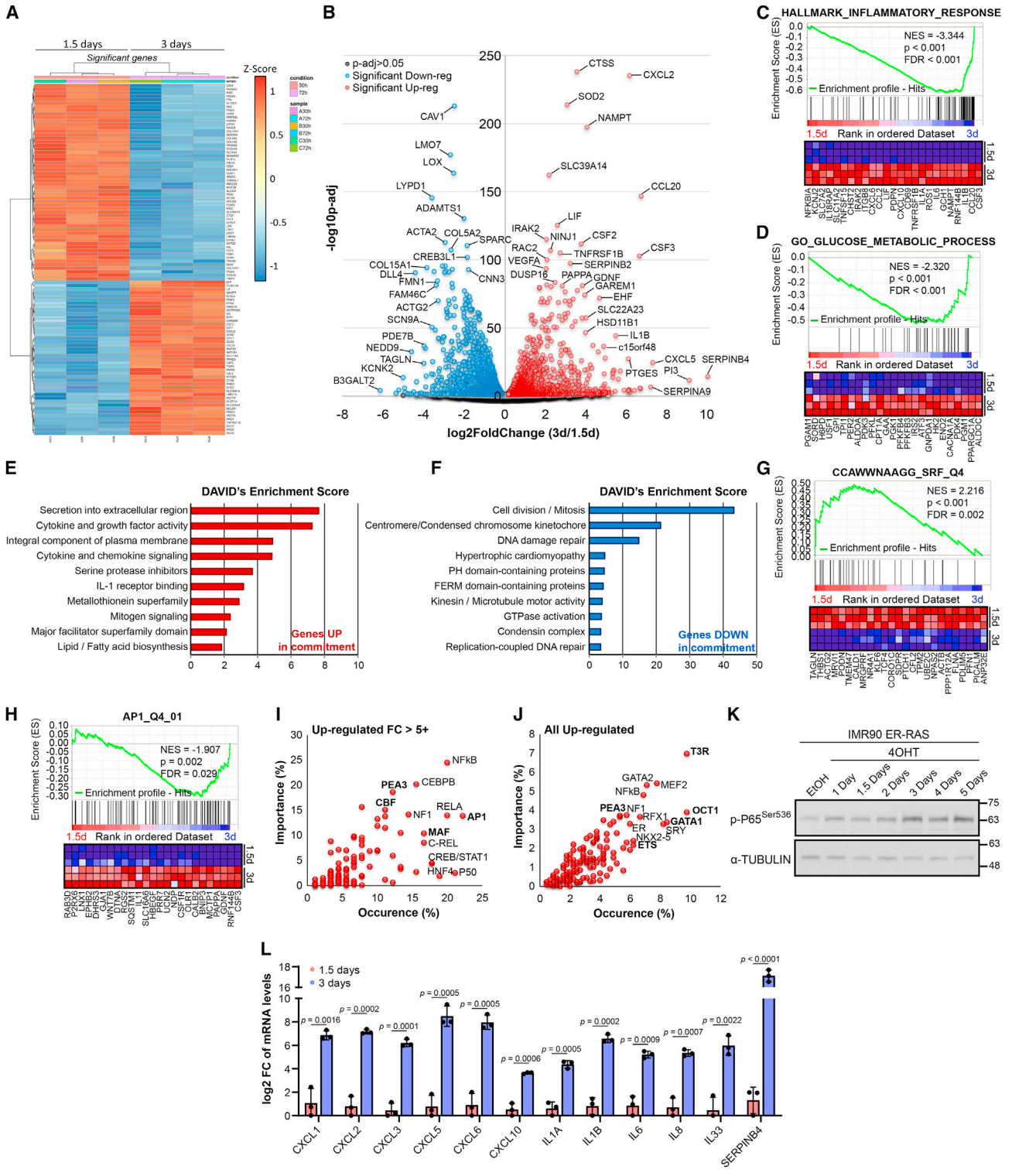

Figure 4. The transcriptome of cells committed to senescence

(A) Heatmap clustering of the top 100 most significant genes based on an adjusted p value (padj) ranking at 30 h (1.5 days) or 72 h (3 days) of ER-RAS activation in IMR90.

(B) Volcano plot of all of the genes in the RNA-seq data. Blue and red, significant genes with padj < 0.01; gray, non-significant genes with padj > 0.01; genes in blue are decreased at 3 days and genes in red are increased at 3 days.

(legend continued on next page)

association with transposons and repeated sequences. Taken together, these results underscore an important role of NADs, LADs, and non-coding regions in the commitment to senescence.

The transcriptome of senescence-committed cells reveals a TF network that regulates senescence

Since the commitment to senescence was linked to the state of the chromatin, we next sought to identify the TFs acting downstream of ERK signaling that regulate the process. We used two strategies to do so. First, we performed motif analysis using HOMER on our ATAC-seq data. HOMER identified several motifs associated with open peaks in committed cells. The most significant motif can be bound by the leucine zipper TFs of the b-ZIP family, including CEBP$\alpha-\delta$, MAFB, HLF, and NFIL3 (Figure 3H). CEBP-β and other TFs of this family have already been linked to senescence.[17] Other motifs have similarities to other TF binding sites, including several senescence regulators such as MNX1,[18] BCL6,[19] NOTCH1/RBPJ, and MEIS1[20]; the IRF family[21]; and SMAD3.[22] Second, we compared the transcriptome of cells where the RAS-ERK pathway was stimulated for 30 h (uncommitted; 1.5 days) with the one from cells stimulated for 72 h (committed; 3 days). Clustering of gene expression using the top 100 most significant genes revealed a clear distinction between cells where RAS-ERK signaling was activated for 1.5 days vs. cells stimulated for 3 days (Figure 4A). Inter- and intragroup variability were assessed both by calculating Pearson's correlation coefficients (Figure S5A) and by PCA (Figure S5B), showing that the gene expression pattern differs between uncommitted and committed cells. The most significant differentially expressed genes are summarized in Figure 4B. Functional annotation of gene expression changes using gene set enrichment analysis (GSEA) and Database for Annotation, Visualization, and Integrated Discovery (DAVID) revealed that the major differences between committed and uncommitted cells concerned factors related to the proinflammatory secretome associated with senescence (SASP) (Figures 4C–4E and S5C–S5E). Intriguingly, the chromatin of genes coding for inflammatory cytokines (SASP) that were found to be highly expressed in committed cells compared to uncommitted cells was open at both cell stages (Figure S4F). This suggests that SASP genes are likely locally primed and opened by a pioneer factor before commitment to RAS-induced senescence and that recruitment of other specific TFs leads to their quick transcription, as is observed with hormone-regulated transcriptional programs.[23,24] Intriguingly, the SASP wave seemed to be temporally centered around the time of commitment (Figures S5F and S5G). Furthermore, among the main signatures for downregulated genes in committed cells was centromere/condensed chromosome (Figure 4F), suggesting decondensation and increased chromatin accessibility, as observed in Figures 2 and 3. Also, committed cells have a reduced expression of genes involved in cell division (Figure 4F) and a high expression of genes in cytokine signaling and metabolism (Figures 4D and 4F).

GSEA revealed that uncommitted cells seemed to rely on a serum response factor (SRF)-dependent transcription known to induce immediate-early genes such as FOS, whereas committed cells seemed to rely on an activator protein 1 (AP1)-dependent transcription (Figures 4G and 4H). Multiple TFs likely controlling these gene expression changes were identified using the bioinformatics platform DiRE (Figures 4I and 4J). Among them, nuclear factor (NF)-κB,[25] CCAAT-enhancer-binding protein (C/EBP),[17,26] AP1,[27] and E26 transformation-specific (ETS) family TF[28] were already linked to senescence. We validated the activation of NF-κB using immunoblots for phosphorylated p65 (Figure 4K) and the expression of several cytokine genes by RT-qPCR (Figure 4L). Overall, the analysis of ATAC-seq and the transcriptome identified a common set of transcriptional regulators of senescence commitment.

To study the role of the TFs linked to commitment, we next interrogated the effects of overexpression or knockdown of those not yet linked to the senescence program. The overexpression of four of these TFs, namely ETV4, RUNX1, OCT1A, and MAFB, induced stable growth arrest (Figure 5A) and multiple senescence biomarkers such as increased SA-β-Gal, p53, retinoblastoma (RB) activation, promyelocytic leukemia (PML) bodies, and SASP, without DNA damage accumulation (Figures 5B–5G) in normal human fibroblasts IMR90. Interestingly, these factors were individually sufficient to promote chromatin opening 3 days after their enforced expression in primary fibroblasts (Figures 5H–5J), suggesting they could play an active role in chromatin opening during the SeRP. Of note, chromatin alterations such as increased accessibility are known to activate ataxia-telangiectasia mutated, and therefore the p53 pathway in the absence of DNA damage.[29–31] It is worth mentioning that the failure to induce senescence by some TFs when overexpressed alone may be due to the lack of partners or posttranslational modifications. Nevertheless, the data are consistent with the activation of a core regulatory network of TFs including but probably not limited to ETV4, RUNX1, OCT1A, and MAFB (Figures S5H and S5I), which initiate senescence. Genes coding for inflammatory cytokines have promoter binding sites for many of these TFs (Figures S5H, S5J, and S5K), explaining why they dominate the differential gene expression profile between committed and non-committed cells. Individual knockdown of

(C and D) GSEA using 1,000 gene set permutations on all of the genes with padj < 0.05.
(E) Functional annotation clustering using DAVID version 6.8 for all significantly upregulated genes at 3 days.
(F) Same as in (E) but for downregulated genes with an FC $\geq$2.
(G and H) GSEA analysis with the same parameters as in (C) and (D).
(I) DiRE analysis for identification of distant regulatory elements performed on upregulated genes with an at least 5-FC and 100 sequencing reads.
(J) Same as in (I) for all upregulated genes with at least 100 reads. DiRE analyses were performed for genes with padj $\leq$ 0.05.
(K) Representative western blot of whole-cell lysates from IMR90 cells expressing ER-RAS and treated with vehicle (EtOH) or 100 nM 4OHT for the indicated period; N = 3.
(L) RT-qPCR for cytokine mRNAs in IMR90 ER-RAS treated for 3 days versus 1.5 days with 100 nM 4OHT. Graphs represent the log2 of mean FC and SD. N = 3, with the mean of each biological replicate indicated by a black dot. An unpaired t test with a 2-tailed p value is indicated.

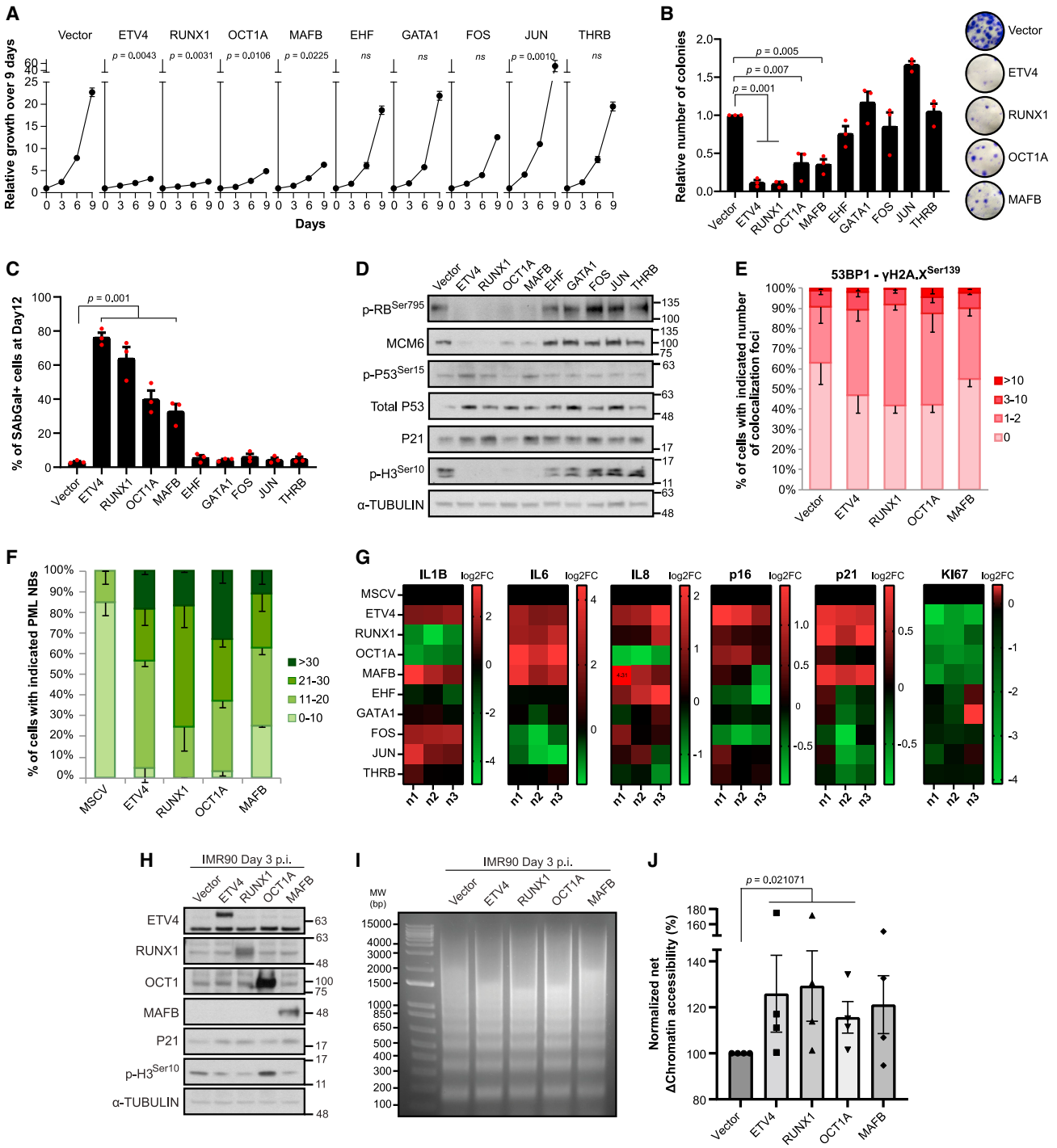

Figure 5. Overexpression of TFs whose signature is enriched during commitment induces senescence

(A) Representative growth curve of IMR90 cells infected with constructs for the overexpression of indicated TFs and plated for experiments at day 7 postinfection. Error bars represent SD. One-way ANOVA with Dunnett's correction, followed by Tukey-HSD were performed, comparing each condition to vector control; N = 3.

(B) Colony assay performed on cells as in (A). Growth was normalized on day 0 from the growth curve plated in parallel. N = 3, with the mean of each biological replicate indicated by a red dot. Error bars represent SEM. One-way ANOVA with Dunnett's correction, followed by Tukey-HSD were performed.

(C) Percentage of SA-β-Gal^{+} cells for conditions as in (A). N = 3, with the mean of each biological replicate indicated by a red dot. Error bars represent SEM. One-way ANOVA with Dunnett's correction, followed by Tukey-HSD were performed.

(D) Representative western blot performed on whole-cell lysates from the same cells as in (A); N = 3.

(legend continued on next page)

these TFs reduced the expression of many cytokine genes (Figure S5L) but did not prevent growth arrest (data not shown), suggesting that they act as a network.

Commitment correlates with chromatin enrichment of the TFs regulating senescence

The dynamics of cells transitioning to a commitment point are consistent with bistable switch mechanisms previously described for oocyte maturation[9] and the mammalian cell-cycle restriction point.[32] The latter depends on positive feedback regulation of the E2F family of TFs.[32] Thus, we next sought to find evidence of sustained expression of the TFs we found regulating the commitment to senescence. At the mRNA level, only MAFB expression increased substantially by the time of commitment (Figure 6A). However, protein levels of ETV4, RUNX1, OCT1, and MAFB increased in chromatin fractions at the time of commitment and remained so, up to 11 days after, when cells were fully senescent (Figure 6B). However, the levels of ETV4 and RUNX1 in whole-cell lysates did not change at the time of commitment (Figure 6C), suggesting that increased binding of senescence-regulating TFs to chromatin links ERK signaling to senescence commitment. Moreover, the levels of both ETV4 and RUNX1 increased at postcommitment times both at the protein and mRNA levels (Figures 6C–6E), suggesting that self-sustaining regulatory loops like those described for the E2F factors maintain cells committed to senescence.[32] We also looked at the localization of ETV4 and RUNX1 in cells that entered RAS-induced senescence and found an increase in their nuclear localization in comparison with control growing cells (Figures 6F and 6G). In cultures of senescent cells, 35 days postinduction of oncogenic RAS expression, some cells spontaneously escape from senescence and regrow. Interestingly, these cells lost the ability to sustain both ETV4 and RUNX1 levels (Figure 6C), suggesting that combined loss of the expression of senescence regulatory TFs may underpin the escape from senescence and malignant transformation.

In multiple cancers, ETV4 and RUNX1 are upregulated,[33,34] raising the question about how senescence is avoided in those tumors. To gain insights into the mechanisms that bypass senescence in cells expressing core senescence TFs, we used the oncoproteins E6 and E7 from the human papillomavirus to disable the p53 and the RB tumor suppressor pathways.[35] Both in IMR90 and MRC5 fibroblasts, either E6 or E7 was sufficient to revert the senescent phenotype. However, E6 had a stronger effect than E7 to inhibit the growth arrest induced by ETV4 (Figures S6A–S6D), suggesting a more important role for p53 activation in maintaining ETV4-induced growth arrest. Also, E6 or E7 alone was less efficient than the combination to revert the senescent phenotype (Figures S6A–S6H), highlighting the capability of ETV4 to activate both pathways.

ETV4 restores senescence in cells that escape from therapy-induced senescence (TIS)

Although senescence is disabled in cancer cells, the process can be restored by anticancer chemotherapy. This TIS is a double-edged sword because in some cases it fuels the emergence of malignant clones that are resistant to chemotherapy.[36] We next asked whether ETV4, acting as a core senescence TF, can restore senescence in cells that escaped from it. Thus, we first induced senescence in the pancreatic cancer cell line KP4 using the drug combination known as FOLFIRINOX.[37] Then, we observed cells that circumvented FIS (FOLFIRINOX-induced senescence) 16 days after cessation of treatment (Figures S7A). FIS was characterized by increased SA-β-Gal, p21, p-ERK, ETV4, RUNX1, and DNA damage (Figures S7B–S7D). Interestingly, the expression levels of ETV4, RUNX1, and p-ERK were increased during the senescent phenotype and returned to basal levels in cells that escaped from FIS (Figure S7C). We then increased ETV4 expression in escapers cells and control cells and rechallenged them with FOLFIRINOX (Figure S7E). As before, FOLFIRINOX induced senescence in control cells but less so in escapers, which became resistant to it. However, upon expression of ETV4 in escapers, the response to FOLFIRINOX was partially restored since many cells reentered senescence and fewer cells escaped from it (Figures S7F–S7I). Finally, we wanted to assess whether chromatin opening mediated by NaBu treatment could potentialize FOLFIRINOX efficiency, thereby increasing the penetrance of the senescent phenotype. To do so, we pretreated cells with either vehicle or NaBu for 24 h, followed by treatment with suboptimal concentrations of the drugs in the FOLFIRINOX regimen (0.35× and 0.5×, compared to the previous 1× experiment). We found that the HDAC inhibitor was able to improve both the growth arrest and the percentage of SA-β-Gal$^+$ cells in FOLFIRINOX-treated cells (Figures S7J–S7L), emphasizing the importance of chromatin opening for tumor suppression.

ETV4 and RUNX1 are highly expressed in premalignant lesions of the pancreas and downregulated in pancreatic adenocarcinomas

To study whether the TF network that mediates commitment to RAS-induced senescence in human fibroblasts plays a role *in vivo* in human cancers, we chose to study pancreatic ductal adenocarcinoma (PDAC). PDAC is initiated by KRAS mutations, and the process of OIS acts as an initial barrier to the progression of these tumors. Low-grade dysplasia of these tumors, known as pancreatic intraepithelial neoplasia (PanIN 1–2), or low-grade intraductal

(E) Quantification of DNA damage foci represented by immunofluorescent colocalization of 53BP1 and γH2A.X in IMR90 cells overexpressing ETV4, RUNX1, OCT1A, or MAFB compared to control vector at day 12 postinfection. N = 2 with SD as error bars (only shown in 1 direction).
(F) Quantification of PML nuclear bodies (PML-NBs) in cells as in (E). Mean of 2 biological replicates is shown, with SD as error bars.
(G) RT-qPCR was performed on the same cells as in (E). Each column represents the mean of a different biological replicate; N= 3.
(H) Representative western blot of whole-cell lysates from IMR90 cells overexpressing ETV4, RUNX1, OCT1A, or MAFB compared to control vector MSCV (murine stem cell virus); N = 2.
(I) Representative MNase assay performed on cells as in (H), at day 3 postinfection; N= 4.
(J) Quantification of MNase assays performed in (I). N = 4 with the mean of each biological replicate identified by a black dot. Error bars represent SEM. Mann-Whitney (Wilcoxon rank-sum) test with continuity correction with a 95% confidence interval using null hypothesis $\mu 0 = \mu 0 = 0.0$ was performed.

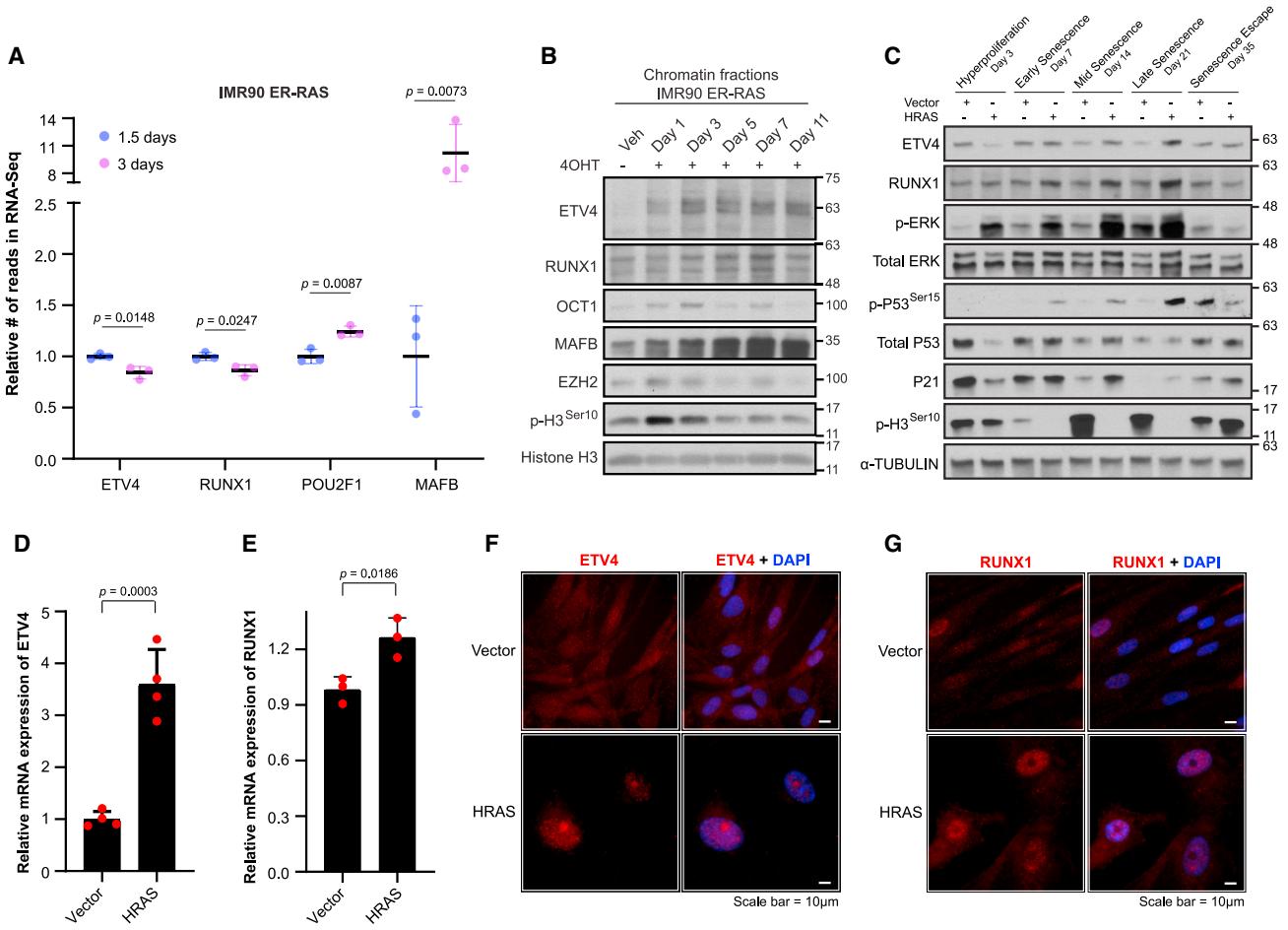

Figure 6. ETV4 and RUNX1 binding to chromatin increases during commitment to senescence, leading to nuclear accumulation and an increase in their levels

(A) Relative number of reads in the RNA-seq data for each of the identified committing TFs. The mean of the 3 biological replicates is shown, with the mean of each replicate as a dot and SD as error bars. An unpaired t test with a 2-tailed p value is indicated.

(B) Representative western blot of purified chromatin fractions from IMR90 cells expressing ER-RAS and treated with vehicle (Veh) for 11 days or with 100 nM 4OHT for 1, 3, 5, 7, or 11 days; N = 2.

(C) Representative western blot with whole-cell lysates from a time course experiment in IMR90 cells expressing constitutive HRAS-G12V or empty control vector; N = 2.

(D and E) ETV4 (D) and (E) RUNX1 mRNA levels measured by RT-qPCR in IMR90 infected with empty control vector or HRAS-G12V. Results shown on day 12 postinfection. N = 4 for ETV4, N = 3 for RUNX1, with SD as error bars for both. An unpaired t test with a 2-tailed p value is indicated.

(F and G) Representative image of immunofluorescence staining for ETV4 and RUNX1 in IMR90 cells expressing control empty vector or constitutive HRAS-G12V for 12 days; N = 3.

papillary mucinous neoplasm (IPMN), contain senescent cells that disappear when they progress to higher-grade dysplasia such as PanIN 3, high-grade IPMN, and PDAC.[5,38–40] Consistent with the presence of senescent cells in low-grade precursors, we found that both ETV4 (Figures 7A–7C) and RUNX1 (Figures 7D–7F) were highly expressed in the nucleus of low-grade IPMN and PanIN cells. As lesions progressed into high-grade dysplasia, both ETV4 and RUNX1 levels were attenuated. Finally, PDAC samples had almost a complete loss of signal of both TFs. Of note, loss of ETV4 and RUNX1 was even more pronounced in poorly differentiated PDAC, which are more aggressive lesions, compared to well-differentiated (WD) PDAC (Figure 7). In addition, ETV4 nuclear localization was lost upon progression to PDAC (Figures 7A and 7B). Further proof that ETV4$^+$ and RUNX1$^+$ cells in benign lesions were senescent was obtained by staining the lesions for p21 (Figures 7A and 7D). Taken together, our results support the idea that changes in chromatin accessibility triggered by TFs such as ETV4 and RUNX1, acting self-sustainably downstream of activated oncogenes, define the commitment to senescence. Furthermore, this chromatin opening acts as a critical component of the protective senescent tumor suppressor response.

DISCUSSION

Our study reveals a cellular mechanism called SeRP, which acts as a checkpoint for integrating signals that could lead to

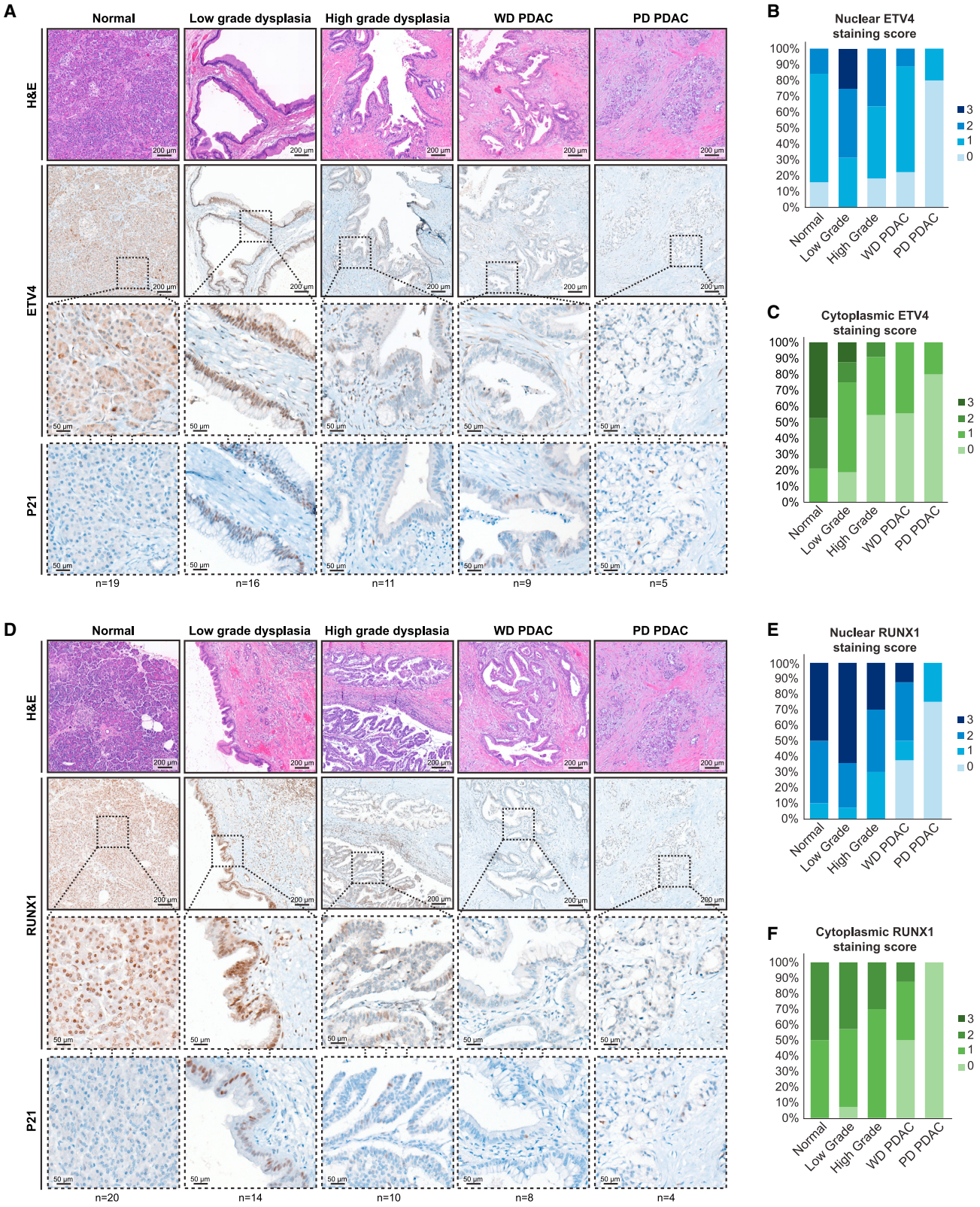

(legend on next page)

malignant transformation. Once cells pass this point, they commit to entering senescence. The transition through the SeRP is akin to a switch, influenced by both the strength and duration of oncogenic signaling. This dual control allows cells to differentiate normal signals from oncogenic ones effectively. The SeRP transition exhibits characteristics of ultrasensitivity, a feature shared with other cellular decision mechanisms such as oocyte maturation in frogs[9] and the cell-cycle restriction point.[32] Ultrasensitive processes suggest molecular memory, enabling cells to integrate and recall previous signaling events.[11] Our findings indicate that cells can retain a memory of aberrant ERK signaling events or integrate oncogenic signals from RAS and MYC oncogenes. This ability is crucial because without it, cells may not trigger senescence when multiple mutations activate moderately signaling pathways that alone are insufficient to induce senescence but together can drive transformation.

We then showed that oncogenic signals leading to senescence commitment did not converge at the level of ERK activation but downstream of it via increasing chromatin accessibility. This finding is in line with the extensive chromatin opening documented in cells already senescent by oncogenic RAS signaling.[41] The genomic locations of the most significantly open chromatin regions during commitment were then identified using ATAC-seq, and they correspond to NADs and LADs, which are gene-poor regions containing repeated sequences. These findings align with a gradual chromatin opening observed in NADs and LADs during serial passage, leading to replicative senescence.[16] They also support findings of chromatin opening and transposon reactivation in senescent cells.[42,43] We suggest that this gradual opening of chromatin is the result of the action of TFs such as C/EBPβ, RBPJ, ETV4, RUNX1, MAFB, and OCT1, which are activated by oncogenic signaling but also sufficient on their own to trigger senescence. Of note, it is also plausible that other reported mechanisms of chromatin opening in senescent cells play a role. These include NOTCH-driven HMGA1 downregulation,[41] downregulation of HMGB2,[44] degradation of HDACs,[45] and DNA hypomethylation.[46] We view chromatin opening as an ultrasensitive process acting at the three-dimensional (3D) ultrastructure level, affecting chromatin topology and homeostasis, and thus disrupting crucial processes that ultimately trigger the SeRP when a certain threshold of chromatin decondensation is reached in regions such as NADs. Indeed, one could imagine that euchromatinization of NADs could affect the phase separation of nucleoli with nucleoplasm that is mediated by perinucleolar heterochromatin composed of NADs.[47,48] This could lead to nucleoli coalescence and impaired ribosome biogenesis,[49] as seen in senescent cells.[35] This view is consistent with previous results showing changes in 3D-chromatin conformation in senescent cells.[44,50,51] Hence, at the cellular level, commitment to senescence may signify the adoption of distinct chromatin structures in response to deregulated TF activity.

We identified TFs that are sufficient to trigger senescence, indicating that they are critical to commit aberrantly stressed cells to senescence. The core TFs for senescence commitment in response to oncogenic RAS we identified here (ETV4, RUNX1, OCT1, and MAFB) and others identified in other laboratories (AP1,[27] NF-κB,[25,52] ETS,[28] and STAT5[53]) are often upregulated in human cancers. We propose that their prosenescence role is linked to their action in recruiting chromatin openers, which disrupt the functions of the heterochromatin[54,55] and activate p53[29–31] and RB,[56–58] the tumor suppressors that execute senescence. Of note, the individual inactivation of the TFs mediating commitment did not inhibit senescence likely because the lack of a single factor can be compensated by others in the network.

Furthermore, cancers may also avoid the prosenescence activity of the TF network by reducing their expression, as shown here in human PDAC samples, by disabling tumor suppressors acting downstream or by reducing chromatin accessibility. Consistent with our proposed role for chromatin opening controlling the SeRP, several histone acetyltransferases[59–61] and histone demethylases are required for senescence.[58,62] Along the same line, several transcriptional repressors can inhibit senescence and are among the most powerful oncogenes found in human cancers.[56,63–65] This raises the question of whether cancer cells avoid triggering the SeRP by disabling their ability to keep a memory of oncogenic threats through modulation of chromatin accessibility. Our work leads us to reconsider current antitumor therapeutic strategies that aim to directly modulate the amplitude of MAPK signaling using inhibitors or agonists. Indeed, since ERK kinases have multiple antagonistic functions in the cell, and their basal levels vary significantly between cell types, such a strategy is likely to have undesirable effects. Consequently, several MAPK pathway inhibitors have been linked to chemoresistance.[66] Therefore, a potentially safer alternative strategy to consider would be to attempt to phenocopy the tumor-suppressive functional consequence associated with the SeRP—an increase in chromatin accessibility, rather than trying to modulate upstream signaling to achieve this effect. This strategy could even be considered in combination with cytotoxic chemotherapeutic agents to increase penetrance of the senescence phenotype.

Limitations of the study

Further understanding chromatin opening during senescence commitment will require mapping key chromatin marks associated with chromatin accessibility. Demonstrating the pivotal role of chromatin opening in senescence will necessitate using

Figure 7. ETV4 and RUNX1 levels are high in human pancreatic benign lesions and decrease in pancreatic ductal adenocarcinoma

(A) Immunohistochemical staining of human pancreatic tissues with anti-ETV4 and anti-p21 antibodies. Normal pancreas and different grades of pancreatic cancer lesions are shown. Insets: enlarged representative regions. The number of patients used for the analysis of each grade is indicated below the inset. PD, poorly differentiated; WD, well differentiated.

(B and C) Scoring of nuclear ETV4 (B) or cytoplasmic (C) staining in epithelial cells from the different patients considered in (A). Four intensities of staining have been considered (0: none; 1: low; 2: moderate; 3: high). The mean percentage of cells for each category of staining intensity is shown in the histogram.

(D) Staining as in (A) but for RUNX1.

(E and F) Nuclear (E) or cytoplasmic (F) staining scoring as in (B) and (C), but for RUNX1 with patients from (D).

an approach that prevents senescence by globally or selectively closing chromatin. The latter could be achieved using CRISPR inhibitor-based methods to catalyze heterochromatin formation at specific loci. In addition, the memory of oncogenic stress described here was only evaluated for a brief period in cell culture. It will be crucial to determine how long cells can retain this memory *in vivo*. Lastly, it is important to map the critical binding sites for TFs that regulate senescence commitment using Cut&Run. The relative contribution of these binding sites in non-coding versus coding regions should be assessed by deleting them using CRISPR.

STAR★METHODS

Detailed methods are provided in the online version of this paper and include the following:

- KEY RESOURCES TABLE
- RESOURCE AVAILABILITY
  - Lead contact
  - Materials availability
  - Data and code availability
- EXPERIMENTAL MODEL AND SUBJECT PARTICIPANT DETAILS
  - Cells
  - Plasmids
- METHOD DETAILS
  - Viral transduction of cells
  - Chromatin fractionation
  - Western-blots
  - MNase assays
  - Cell proliferation assay
  - SA-β-gal assay
  - Histology and immunohistochemistry
  - Immunofluorescence and FACS analysis
  - RT-qPCR
  - ATAC-seq
  - RNA-seq: Library preparation for RNA-Sequencing and data analysis
  - Analysis of the dynamics of commitment
- QUANTIFICATION AND STATISTICAL ANALYSIS

SUPPLEMENTAL INFORMATION

Supplemental information can be found online at https://doi.org/10.1016/j.celrep.2024.114044.

ACKNOWLEDGMENTS

We thank Jennifer Huber, Patrick Gendron (IRIC), and Gaspard Reulet (Montreal Clinical Research Institute [IRCM]) for omics analysis. We thank Liliane Meunier and Véronique Barrès from the the pathology platform at the CRCHUM and Louise Rousseau for biospecimen and related data handling at the Center Hospitalier de l'Université de Montréal Hepatopancreatobiliary Biobank and Database, accredited by the Canadian Tissue Repository Network, led by S.T. Work was supported by the Canadian Institutes of Health Research (CIHR) MCC 419348 and the Terry Fox Research Institute 1123. S.L.-P. is supported by FRQS (Fonds de Recherche du Québec-Santé) and the CIHR. S.T. is supported by the Université de Montréal Roger Des-Groseillers Research Chair in Hepatopancreatobiliary Surgical Oncology, the FRQS clinician scientist Junior 2 grant 298832. S.L.-P., M.-C.R., J.G., and P.K. were supported by funds from the Institut du Cancer de Montréal and the Défi Canderel. G.F. is supported by the CIBC Chair for Breast Cancer Research.

AUTHOR CONTRIBUTIONS

S.L.-P. designed the experiments and performed most of the experiments, including cell culture experiments, growth assays, western blots, RT-qPCR, immunofluorescence, MNase assays, SA-β-Gal, chromatin fractionation, and data analysis. V.B. performed experiments in Figures 1I–1L and S1G, additional biological replicates for Figures 2M, 2N, and S3, and cloned TFs used in Figure 5. M.-C.R. performed experiments that were not included in the final version of this article and helped design and perform cell culture experiments. D.A.M. performed bioinformatic analysis of ATAC-seq data in collaboration with G.F. at IRCM. J.G. performed western blots with samples generated by S.L.-P. for Figures S1C, S1F, S7H, and S7I. P.K. repeated western blots performed by J.G. with other biological replicates. A.B. and A.S. conducted the mathematical analysis of bistability and generated panels of Figures 1M and 1N. V.Q.-H.T. and F.A. (pathologists) analyzed and scored immunohistochemistry (IHC) in Figure 7. S.T. provided biospecimens and related data, associated funding, critical input on data, and the manuscript. S.L.-P. and G.F. wrote the manuscript. All of the authors revised the final manuscript.

DECLARATION OF INTERESTS

The authors declare no competing interests.

Received: December 14, 2022
Revised: February 12, 2024
Accepted: March 19, 2024

REFERENCES

1. Pardee, A.B. (1974). A restriction point for control of normal animal cell proliferation. Proc. Natl. Acad. Sci. USA *71*, 1286–1290. https://doi.org/10.1073/pnas.71.4.1286.
2. Sherr, C.J., Beach, D., and Shapiro, G.I. (2016). Targeting CDK4 and CDK6: From Discovery to Therapy. Cancer Discov. *6*, 353–367. https://doi.org/10.1158/2159-8290.CD-15-0894.
3. Deschênes-Simard, X., Gaumont-Leclerc, M.F., Bourdeau, V., Lessard, F., Moiseeva, O., Forest, V., Igelmann, S., Mallette, F.A., Saba-El-Leil, M.K., Meloche, S., et al. (2013). Tumor suppressor activity of the ERK/MAPK pathway by promoting selective protein degradation. Genes Dev. *27*, 900–915. https://doi.org/10.1101/gad.203984.112.
4. Deschênes-Simard, X., Kottakis, F., Meloche, S., and Ferbeyre, G. (2014). ERKs in cancer: friends or foes? Cancer Res. *74*, 412–419. https://doi.org/10.1158/0008-5472.CAN-13-2381.
5. Caldwell, M.E., DeNicola, G.M., Martins, C.P., Jacobetz, M.A., Maitra, A., Hruban, R.H., and Tuveson, D.A. (2012). Cellular features of senescence during the evolution of human and murine ductal pancreatic cancer. Oncogene *31*, 1599–1608. https://doi.org/10.1038/onc.2011.350.
6. Sethi, V., Giri, B., Saluja, A., and Dudeja, V. (2017). Insights into the Pathogenesis of Pancreatic Cystic Neoplasms. Dig. Dis. Sci. *62*, 1778–1786. https://doi.org/10.1007/s10620-017-4603-1.
7. Sarkisian, C.J., Keister, B.A., Stairs, D.B., Boxer, R.B., Moody, S.E., and Chodosh, L.A. (2007). Dose-dependent oncogene-induced senescence in vivo and its evasion during mammary tumorigenesis. Nat. Cell Biol. *9*, 493–505.
8. Santos, S.D.M., Verveer, P.J., and Bastiaens, P.I.H. (2007). Growth factor-induced MAPK network topology shapes Erk response determining PC-12 cell fate. Nat. Cell Biol. *9*, 324–330. https://doi.org/10.1038/ncb1543.

9. Xiong, W., and Ferrell, J.E., Jr. (2003). A positive-feedback-based bistable 'memory module' that governs a cell fate decision. Nature *426*, 460–465. https://doi.org/10.1038/nature02089.

10. Mojtahedi, M., Skupin, A., Zhou, J., Castano, I.G., Leong-Quong, R.Y., Chang, H., Trachana, K., Giuliani, A., and Huang, S. (2016). Cell Fate Decision as High-Dimensional Critical State Transition. PLoS Biol. *14*, e2000640. https://doi.org/10.1371/journal.pbio.2000640.

11. Pomerening, J.R., Sontag, E.D., and Ferrell, J.E., Jr. (2003). Building a cell cycle oscillator: hysteresis and bistability in the activation of Cdc2. Nat. Cell Biol. *5*, 346–351. https://doi.org/10.1038/ncb954.

12. Nie, Z., Hu, G., Wei, G., Cui, K., Yamane, A., Resch, W., Wang, R., Green, D.R., Tessarollo, L., Casellas, R., et al. (2012). c-Myc is a universal amplifier of expressed genes in lymphocytes and embryonic stem cells. Cell *151*, 68–79. https://doi.org/10.1016/j.cell.2012.08.033.

13. Esnault, C., Gualdrini, F., Horswell, S., Kelly, G., Stewart, A., East, P., Matthews, N., and Treisman, R. (2017). ERK-Induced Activation of TCF Family of SRF Cofactors Initiates a Chromatin Modification Cascade Associated with Transcription. Mol. Cell *65*, 1081–1095.e5. https://doi.org/10.1016/j.molcel.2017.02.005.

14. Ruley, H.E. (1983). Adenovirus early region 1A enables viral and cellular transforming genes to transform primary cells in culture. Nature *304*, 602–606.

15. Zindy, F., Eischen, C.M., Randle, D.H., Kamijo, T., Cleveland, J.L., Sherr, C.J., and Roussel, M.F. (1998). Myc signaling via the ARF tumor suppressor regulates p53-dependent apoptosis and immortalization. Genes Dev. *12*, 2424–2433.

16. Chan, M., Yuan, H., Soifer, I., Maile, T.M., Wang, R.Y., Ireland, A., O'Brien, J.J., Goudeau, J., Chan, L.J.G., Vijay, T., et al. (2022). Novel insights from a multiomics dissection of the Hayflick limit. Elife *11*, e70283. https://doi.org/10.7554/eLife.70283.

17. Acosta, J.C., O'Loghlen, A., Banito, A., Guijarro, M.V., Augert, A., Raguz, S., Fumagalli, M., Da Costa, M., Brown, C., Popov, N., et al. (2008). Chemokine signaling via the CXCR2 receptor reinforces senescence. Cell *133*, 1006–1018.

18. Ingenhag, D., Reister, S., Auer, F., Bhatia, S., Wildenhain, S., Picard, D., Remke, M., Hoell, J.I., Kloetgen, A., Sohn, D., et al. (2019). The homeobox transcription factor HB9 induces senescence and blocks differentiation in hematopoietic stem and progenitor cells. Haematologica *104*, 35–46. https://doi.org/10.3324/haematol.2018.189407.

19. Ranuncolo, S.M., Wang, L., Polo, J.M., Dell'Oso, T., Dierov, J., Gaymes, T.J., Rassool, F., Carroll, M., and Melnick, A. (2008). BCL6-mediated attenuation of DNA damage sensing triggers growth arrest and senescence through a p53-dependent pathway in a cell context-dependent manner. J. Biol. Chem. *283*, 22565–22572. https://doi.org/10.1074/jbc.M803490200.

20. Hoare, M., Ito, Y., Kang, T.W., Weekes, M.P., Matheson, N.J., Patten, D.A., Shetty, S., Parry, A.J., Menon, S., Salama, R., et al. (2016). NOTCH1 mediates a switch between two distinct secretomes during senescence. Nat. Cell Biol. *18*, 979–992. https://doi.org/10.1038/ncb3397.

21. Li, Q., Tang, L., Roberts, P.C., Kraniak, J.M., Fridman, A.L., Kulaeva, O.I., Tehrani, O.S., and Tainsky, M.A. (2008). Interferon regulatory factors IRF5 and IRF7 inhibit growth and induce senescence in immortal Li-Fraumeni fibroblasts. Mol. Cancer Res. *6*, 770–784. https://doi.org/10.1158/1541-7786.MCR-07-0114.

22. Liu, X., Li, X., Wang, S., Liu, Q., Feng, X., Wang, W., Huang, Z., Huang, Y., Wu, J., Cai, M., et al. (2023). ATOH8 binds SMAD3 to induce cellular senescence and prevent Ras-driven malignant transformation. Proc. Natl. Acad. Sci. USA *120*, e2208927120. https://doi.org/10.1073/pnas.2208927120.

23. Carroll, J.S., Liu, X.S., Brodsky, A.S., Li, W., Meyer, C.A., Szary, A.J., Eeckhoute, J., Shao, W., Hestermann, E.V., Geistlinger, T.R., et al. (2005). Chromosome-wide mapping of estrogen receptor binding reveals long-range regulation requiring the forkhead protein FoxA1. Cell *122*, 33–43. https://doi.org/10.1016/j.cell.2005.05.008.

24. Lupien, M., Eeckhoute, J., Meyer, C.A., Wang, Q., Zhang, Y., Li, W., Carroll, J.S., Liu, X.S., and Brown, M. (2008). FoxA1 translates epigenetic signatures into enhancer-driven lineage-specific transcription. Cell *132*, 958–970.

25. Chien, Y., Scuoppo, C., Wang, X., Fang, X., Balgley, B., Bolden, J.E., Premsrirut, P., Luo, W., Chicas, A., Lee, C.S., et al. (2011). Control of the senescence-associated secretory phenotype by NF-kappaB promotes senescence and enhances chemosensitivity. Genes Dev. *25*, 2125–2136. https://doi.org/10.1101/gad.17276711.

26. Sebastian, T., Malik, R., Thomas, S., Sage, J., and Johnson, P.F. (2005). C/EBPbeta cooperates with RB:E2F to implement Ras(V12)-induced cellular senescence. EMBO J. *24*, 3301–3312.

27. Martínez-Zamudio, R.I., Roux, P.F., de Freitas, J.A.N.L.F., Robinson, L., Doré, G., Sun, B., Belenki, D., Milanovic, M., Herbig, U., Schmitt, C.A., et al. (2020). AP-1 imprints a reversible transcriptional programme of senescent cells. Nat. Cell Biol. *22*, 842–855. https://doi.org/10.1038/s41556-020-0529-5.

28. Ohtani, N., Zebedee, Z., Huot, T.J., Stinson, J.A., Sugimoto, M., Ohashi, Y., Sharrocks, A.D., Peters, G., and Hara, E. (2001). Opposing effects of Ets and Id proteins on p16INK4a expression during cellular senescence. Nature *409*, 1067–1070.

29. Bakkenist, C.J., and Kastan, M.B. (2003). DNA damage activates ATM through intermolecular autophosphorylation and dimer dissociation. Nature *421*, 499–506.

30. Kim, Y.C., Gerlitz, G., Furusawa, T., Catez, F., Nussenzweig, A., Oh, K.S., Kraemer, K.H., Shiloh, Y., and Bustin, M. (2009). Activation of ATM depends on chromatin interactions occurring before induction of DNA damage. Nat. Cell Biol. *11*, 92–96. https://doi.org/10.1038/ncb1817.

31. Ji, S., Zhu, L., Gao, Y., Zhang, X., Yan, Y., Cen, J., Li, R., Zeng, R., Liao, L., Hou, C., et al. (2017). Baf60b-mediated ATM-p53 activation blocks cell identity conversion by sensing chromatin opening. Cell Res. *27*, 642–656. https://doi.org/10.1038/cr.2017.36.

32. Yao, G., Lee, T.J., Mori, S., Nevins, J.R., and You, L. (2008). A bistable Rb-E2F switch underlies the restriction point. Nat. Cell Biol. *10*, 476–482. https://doi.org/10.1038/ncb1711.

33. Qi, T., Qu, Q., Li, G., Wang, J., Zhu, H., Yang, Z., Sun, Y., Lu, Q., and Qu, J. (2020). Function and regulation of the PEA3 subfamily of ETS transcription factors in cancer. Am. J. Cancer Res. *10*, 3083–3105.

34. Lin, T.C. (2022). RUNX1 and cancer. Biochim. Biophys. Acta Rev. Canc *1877*, 188715. https://doi.org/10.1016/j.bbcan.2022.188715.

35. Lessard, F., Igelmann, S., Trahan, C., Huot, G., Saint-Germain, E., Mignacca, L., Del Toro, N., Lopes-Paciencia, S., Le Calvé, B., Montero, M., et al. (2018). Senescence-associated ribosome biogenesis defects contributes to cell cycle arrest through the Rb pathway. Nat. Cell Biol. *20*, 789–799. https://doi.org/10.1038/s41556-018-0127-y.

36. Milanovic, M., Fan, D.N.Y., Belenki, D., Däbritz, J.H.M., Zhao, Z., Yu, Y., Dörr, J.R., Dimitrova, L., Lenze, D., Monteiro Barbosa, I.A., et al. (2018). Senescence-associated reprogramming promotes cancer stemness. Nature *553*, 96–100. https://doi.org/10.1038/nature25167.

37. Rowell, M.C., Deschenes-Simard, X., Lopes-Paciencia, S., Le Calve, B., Kalegari, P., Mignacca, L., Fernandez-Ruiz, A., Guillon, J., Lessard, F., Bourdeau, V., et al. (2023). Targeting Ribosome Biogenesis Reinforces ERK-dependent Senescence in Pancreatic Cancer (Cell cycle), pp. 1–22. https://doi.org/10.1080/15384101.2023.2278945.

38. Carrière, C., Gore, A.J., Norris, A.M., Gunn, J.R., Young, A.L., Longnecker, D.S., and Korc, M. (2011). Deletion of Rb accelerates pancreatic carcinogenesis by oncogenic Kras and impairs senescence in premalignant lesions. Gastroenterology *141*, 1091–1101. https://doi.org/10.1053/j.gastro.2011.05.041.

39. Deschênes-Simard, X., Parisotto, M., Rowell, M.C., Le Calvé, B., Igelmann, S., Moineau-Vallée, K., Saint-Germain, E., Kalegari, P., Bourdeau, V., Kottakis, F., et al. (2019). Circumventing senescence is associated

with stem cell properties and metformin sensitivity. Aging Cell *18*, e12889. https://doi.org/10.1111/acel.12889.

40. Guerra, C., Collado, M., Navas, C., Schuhmacher, A.J., Hernández-Porras, I., Cañamero, M., Rodriguez-Justo, M., Serrano, M., and Barbacid, M. (2011). Pancreatitis-induced inflammation contributes to pancreatic cancer by inhibiting oncogene-induced senescence. Cancer Cell *19*, 728–739. https://doi.org/10.1016/j.ccr.2011.05.011.
41. Parry, A.J., Hoare, M., Bihary, D., Hänsel-Hertsch, R., Smith, S., Tomimatsu, K., Mannion, E., Smith, A., D'Santos, P., Russell, I.A., et al. (2018). NOTCH-mediated non-cell autonomous regulation of chromatin structure during senescence. Nat. Commun. *9*, 1840. https://doi.org/10.1038/s41467-018-04283-9.
42. De Cecco, M., Ito, T., Petrashen, A.P., Elias, A.E., Skvir, N.J., Criscione, S.W., Caligiana, A., Brocculi, G., Adney, E.M., Boeke, J.D., et al. (2019). L1 drives IFN in senescent cells and promotes age-associated inflammation. Nature *566*, 73–78. https://doi.org/10.1038/s41586-018-0784-9.
43. De Cecco, M., Criscione, S.W., Peckham, E.J., Hillenmeyer, S., Hamm, E.A., Manivannan, J., Peterson, A.L., Kreiling, J.A., Neretti, N., and Sedivy, J.M. (2013). Genomes of replicatively senescent cells undergo global epigenetic changes leading to gene silencing and activation of transposable elements. Aging Cell *12*, 247–256. https://doi.org/10.1111/acel.12047.
44. Zirkel, A., Nikolic, M., Sofiadis, K., Mallm, J.P., Brackley, C.A., Gothe, H., Drechsel, O., Becker, C., Altmüller, J., Josipovic, N., et al. (2018). HMGB2 Loss upon Senescence Entry Disrupts Genomic Organization and Induces CTCF Clustering across Cell Types. Mol. Cell *70*, 730–744.e6. https://doi.org/10.1016/j.molcel.2018.03.030.
45. Di Giorgio, E., Paluvai, H., Dalla, E., Ranzino, L., Renzini, A., Moresi, V., Minisini, M., Picco, R., and Brancolini, C. (2021). HDAC4 degradation during senescence unleashes an epigenetic program driven by AP-1/p300 at selected enhancers and super-enhancers. Genome Biol. *22*, 129. https://doi.org/10.1186/s13059-021-02340-z.
46. Cruickshanks, H.A., McBryan, T., Nelson, D.M., Vanderkraats, N.D., Shah, P.P., van Tuyn, J., Singh Rai, T., Brock, C., Donahue, G., Dunican, D.S., et al. (2013). Senescent cells harbour features of the cancer epigenome. Nat. Cell Biol. *15*, 1495–1506. https://doi.org/10.1038/ncb2879.
47. Caragine, C.M., Haley, S.C., and Zidovska, A. (2019). Nucleolar dynamics and interactions with nucleoplasm in living cells. Elife *8*, e47533. https://doi.org/10.7554/eLife.47533.
48. Lafontaine, D.L.J., Riback, J.A., Bascetin, R., and Brangwynne, C.P. (2021). The nucleolus as a multiphase liquid condensate. Nat. Rev. Mol. Cell Biol. *22*, 165–182. https://doi.org/10.1038/s41580-020-0272-6.
49. Yu, H., Sun, Z., Tan, T., Pan, H., Zhao, J., Zhang, L., Chen, J., Lei, A., Zhu, Y., Chen, L., et al. (2021). rRNA biogenesis regulates mouse 2C-like state by 3D structure reorganization of peri-nucleolar heterochromatin. Nat. Commun. *12*, 6365. https://doi.org/10.1038/s41467-021-26576-2.
50. Chandra, T., Ewels, P.A., Schoenfelder, S., Furlan-Magaril, M., Wingett, S.W., Kirschner, K., Thuret, J.Y., Andrews, S., Fraser, P., and Reik, W. (2015). Global reorganization of the nuclear landscape in senescent cells. Cell Rep. *10*, 471–483. https://doi.org/10.1016/j.celrep.2014.12.055.
51. Iwasaki, O., Tanizawa, H., Kim, K.D., Kossenkov, A., Nacarelli, T., Tashiro, S., Majumdar, S., Showe, L.C., Zhang, R., and Noma, K.I. (2019). Involvement of condensin in cellular senescence through gene regulation and compartmental reorganization. Nat. Commun. *10*, 5688. https://doi.org/10.1038/s41467-019-13604-5.
52. Jing, H., Kase, J., Dörr, J.R., Milanovic, M., Lenze, D., Grau, M., Beuster, G., Ji, S., Reimann, M., Lenz, P., et al. (2011). Opposing roles of NF-kappaB in anti-cancer treatment outcome unveiled by cross-species investigations. Genes Dev. *25*, 2137–2146. https://doi.org/10.1101/gad.17620611.
53. Mallette, F.A., Gaumont-Leclerc, M.F., Huot, G., and Ferbeyre, G. (2007). Myc down-regulation as a mechanism to activate the Rb pathway in STAT5A-induced senescence. J. Biol. Chem. *282*, 34938–34944. https://doi.org/10.1074/jbc.M707074200.
54. Diao, Z., Ji, Q., Wu, Z., Zhang, W., Cai, Y., Wang, Z., Hu, J., Liu, Z., Wang, Q., Bi, S., et al. (2021). SIRT3 consolidates heterochromatin and counteracts senescence. Nucleic Acids Res. *49*, 4203–4219. https://doi.org/10.1093/nar/gkab161.
55. Miyata, K., Imai, Y., Hori, S., Nishio, M., Loo, T.M., Okada, R., Yang, L., Nakadai, T., Maruyama, R., Fujii, R., et al. (2021). Pericentromeric noncoding RNA changes DNA binding of CTCF and inflammatory gene expression in senescence and cancer. Proc. Natl. Acad. Sci. USA *118*, e2025647118. https://doi.org/10.1073/pnas.2025647118.
56. Bracken, A.P., Kleine-Kohlbrecher, D., Dietrich, N., Pasini, D., Gargiulo, G., Beekman, C., Theilgaard-Mönch, K., Minucci, S., Porse, B.T., Marine, J.C., et al. (2007). The Polycomb group proteins bind throughout the INK4A-ARF locus and are disassociated in senescent cells. Genes Dev. *21*, 525–530.
57. Shah, P.P., Donahue, G., Otte, G.L., Capell, B.C., Nelson, D.M., Cao, K., Aggarwala, V., Cruickshanks, H.A., Rai, T.S., McBryan, T., et al. (2013). Lamin B1 depletion in senescent cells triggers large-scale changes in gene expression and the chromatin landscape. Genes Dev. *27*, 1787–1799. https://doi.org/10.1101/gad.223834.113.
58. Agger, K., Cloos, P.A.C., Rudkjaer, L., Williams, K., Andersen, G., Christensen, J., and Helin, K. (2009). The H3K27me3 demethylase JMJD3 contributes to the activation of the INK4A-ARF locus in response to oncogene- and stress-induced senescence. Genes Dev. *23*, 1171–1176. https://doi.org/10.1101/gad.510809.
59. Huang, B., Zhong, D., Zhu, J., An, Y., Gao, M., Zhu, S., Dang, W., Wang, X., Yang, B., and Xie, Z. (2020). Inhibition of histone acetyltransferase GCN5 extends lifespan in both yeast and human cell lines. Aging Cell *19*, e13129. https://doi.org/10.1111/acel.13129.
60. Sen, P., Lan, Y., Li, C.Y., Sidoli, S., Donahue, G., Dou, Z., Frederick, B., Chen, Q., Luense, L.J., Garcia, B.A., et al. (2019). Histone Acetyltransferase p300 Induces De Novo Super-Enhancers to Drive Cellular Senescence. Mol. Cell *73*, 684–698.e8. https://doi.org/10.1016/j.molcel.2019.01.021.
61. Zheng, H., Seit-Nebi, A., Han, X., Aslanian, A., Tat, J., Liao, R., Yates, J.R., 3rd, and Sun, P. (2013). A posttranslational modification cascade involving p38, Tip60, and PRAK mediates oncogene-induced senescence. Mol. Cell *50*, 699–710. https://doi.org/10.1016/j.molcel.2013.04.013.
62. Zhang, B., Long, Q., Wu, S., Xu, Q., Song, S., Han, L., Qian, M., Ren, X., Liu, H., Jiang, J., et al. (2021). KDM4 Orchestrates Epigenomic Remodeling of Senescent Cells and Potentiates the Senescence-Associated Secretory Phenotype. Nat. Aging *1*, 454–472. https://doi.org/10.1038/s43587-021-00063-1.
63. Xia, L., Huang, W., Bellani, M., Seidman, M.M., Wu, K., Fan, D., Nie, Y., Cai, Y., Zhang, Y.W., Yu, L.R., et al. (2017). CHD4 Has Oncogenic Functions in Initiating and Maintaining Epigenetic Suppression of Multiple Tumor Suppressor Genes. Cancer Cell *31*, 653–668.e7. https://doi.org/10.1016/j.ccell.2017.04.005.
64. Ito, T., Teo, Y.V., Evans, S.A., Neretti, N., and Sedivy, J.M. (2018). Regulation of Cellular Senescence by Polycomb Chromatin Modifiers through Distinct DNA Damage- and Histone Methylation-Dependent Pathways. Cell Rep. *22*, 3480–3492. https://doi.org/10.1016/j.celrep.2018.03.002.
65. Baumann, C., Zhang, X., and De La Fuente, R. (2020). Loss of CBX2 induces genome instability and senescence-associated chromosomal rearrangements. J. Cell Biol. *219*, e201910149. https://doi.org/10.1083/jcb.201910149.
66. Viale, A., Pettazzoni, P., Lyssiotis, C.A., Ying, H., Sánchez, N., Marchesini, M., Carugo, A., Green, T., Seth, S., Giuliani, V., et al. (2014). Oncogene ablation-resistant pancreatic cancer cells depend on mitochondrial function. Nature *514*, 628–632. https://doi.org/10.1038/nature13611.
67. Paddison, P.J., Cleary, M., Silva, J.M., Chang, K., Sheth, N., Sachidanandam, R., and Hannon, G.J. (2004). Cloning of short hairpin RNAs for gene knockdown in mammalian cells. Nat. Methods *1*, 163–167. https://doi.org/10.1038/nmeth1104-163.

68. Gillotin, S., Davies, J.D., and Philpott, A. (2018). Subcellular localisation modulates ubiquitylation and degradation of Ascl1. Sci. Rep. *8*, 4625. https://doi.org/10.1038/s41598-018-23056-4.

69. Igelmann, S., Lessard, F., Uchenunu, O., Bouchard, J., Fernandez-Ruiz, A., Rowell, M.C., Lopes-Paciencia, S., Papadopoli, D., Fouillen, A., Ponce, K.J., et al. (2021). A hydride transfer complex reprograms NAD metabolism and bypasses senescence. Mol. Cell *81*, 3848–3865.e19. https://doi.org/10.1016/j.molcel.2021.08.028.

70. Bolger, A.M., Lohse, M., and Usadel, B. (2014). Trimmomatic: a flexible trimmer for Illumina sequence data. Bioinformatics *30*, 2114–2120. https://doi.org/10.1093/bioinformatics/btu170.

71. Dobin, A., Davis, C.A., Schlesinger, F., Drenkow, J., Zaleski, C., Jha, S., Batut, P., Chaisson, M., and Gingeras, T.R. (2013). STAR: ultrafast universal RNA-seq aligner. Bioinformatics *29*, 15–21. https://doi.org/10.1093/bioinformatics/bts635.

72. Li, B., and Dewey, C.N. (2011). RSEM: accurate transcript quantification from RNA-Seq data with or without a reference genome. BMC Bioinf. *12*, 323. https://doi.org/10.1186/1471-2105-12-323.

73. Love, M.I., Huber, W., and Anders, S. (2014). Moderated estimation of fold change and dispersion for RNA-seq data with DESeq2. Genome Biol. *15*, 550. https://doi.org/10.1186/s13059-014-0550-8.

74. Subramanian, A., Tamayo, P., Mootha, V.K., Mukherjee, S., Ebert, B.L., Gillette, M.A., Paulovich, A., Pomeroy, S.L., Golub, T.R., Lander, E.S., and Mesirov, J.P. (2005). Gene set enrichment analysis: a knowledge-based approach for interpreting genome-wide expression profiles. Proc. Natl. Acad. Sci. USA *102*, 15545–15550. https://doi.org/10.1073/pnas.0506580102.

STAR★METHODS

KEY RESOURCES TABLE

REAGENT or RESOURCE	SOURCE	IDENTIFIER
Antibodies		
p21 mouse monoclonal	BD Pharmingen	Cat# 556431; RRID:AB_396415
MCM6 rabbit polyclonal	Bethyl Laboratories	Cat# A300-194A; RRID:AB_162727
Phospho-ERK 1/2 (p44/p42) Thr202/Tyr204, rabbit polyclonal	Cell Signaling	Cat#4370; RRID:AB_2315112
ERK rabbit polyclonal	Cell Signaling	Cat#9102; RRID:AB_330744
Phospho-P90/RSK	Santa Cruz	sc-377526
α-TUBULIN mouse monoclonal	Sigma-Aldrich	Cat#T6074; RRID:AB_477582
Phospho-RBS795 rabbit polyclonal	Cell Signaling	Cat# 9301; RRID:AB_330013
Phospho-p53S15 rabbit polyclonal	Cell Signaling	Cat# 9284; RRID:AB_331464
Total P53 mouse monoclonal	Santa Cruz	Sc-126; RRID:AB_628082
Phospho-H3S10 rabbit polyclonal	Millipore	Cat# 06–570; RRID:AB_310177
Phospho-NF-κB P65 Ser536 rabbit monoclonal	Cell Signaling	Cat#3033; RRID:AB_331284
ETV4 rabbit polyclonal	Abcam	ab189826
RUNX1 Rabbit polyclonal	Abcam	ab23980; RRID:AB_2184205
OCT1 mouse monoclonal	Santa Cruz	sc-8024; RRID:AB_628049
MAFB mouse monoclonal	Santa Cruz	sc-376387; RRID:AB_10988929
EZH2 rabbit polyclonal	Cell Signaling	Cat#5246; RRID:AB_10694683
Phospho-*c*-RAF (Ser338) rabbit monoclonal	Cell Signaling	Cat#9427; RRID:AB_2067317
RAF1 rabbit polyclonal	Santa Cruz	sc-133; RRID:AB_632305
MEK rabbit polyclonal	Cell Signaling	Cat#9122; RRID:AB_823567
Phospho-MEK 1/2 (Ser217/221) rabbit polyclonal	Cell Signaling	Cat#9121; RRID:AB_331648
DUSP6 rabbit monoclonal	Abcam	ab76310; RRID:AB_1523517
c-MYC rabbit polyclonal	Santa Cruz	sc-789; RRID:AB_631274
ERα rabbit polyclonal	Santa Cruz	sc-543; RRID:AB_631471
Histone H3 rabbit polyclonal	Abcam	Cat#ab1791; RRID:AB_302613
Goat anti-rabbit IgG (H-L) conjugated to HRP	Bio-Rad	Cat# 170–6515; RRID:AB_11125142
Goat anti-mouse IgG (H-L) conjugated to HRP	Bio-Rad	Cat# 170–6516 RRID:AB_11125547
anti-H-RAS mouse monoclonal	Santa Cruz Biotechnology	Cat#Sc29; RRID:AB_627750
53BP1 rabbit polyclonal	Calbiochem	Cat# PC712; RRID:AB_564982
Phospho-gammaH2A.XS139 mouse monoclonal	Millipore	Cat# 05-636-I; RRID:AB_2755003

(*Continued on next page*)

Continued

REAGENT or RESOURCE	SOURCE	IDENTIFIER
ETV4 rabbit polyclonal	Invitrogen	PA5-99226; RRID:AB_2818159
PML rabbit polyclonal	Bethyl Laboratories	Cat# A301-167A; RRID:AB_873108
Biological samples		
Normal and neoplastic pancreatic tissue	CHUM Hepato-pancreatobiliary Cancer Biobank	This study
Chemicals, peptides, and recombinant proteins		
Crystal Violet	Bioshop	Cat # CRY 422.100
4-Hydroxytamoxifen	Sigma-Aldrich	Cat# H7904
SCH772984	Selleckchem	Cat# S7101
AZD6244	Selleckchem	Cat# S1008
oxaliplatin	Selleckchem	Cat# S1224
5-Fluorouracil (5FU)	Selleckchem	Cat# S1209
Sn38 (irinotecan)	Selleckchem	Cat# S4908
DAPI (4′,6-Diamidino-2-Phenylindole, Dihydrochloride)	Invitrogen/Thermo Fisher Scientific	Cat #D1306
Potassium hexacyanoferrate(II) trihydrate	Sigma-Aldrich	Cat #P3289
Potassium ferricyanide(III)	Sigma-Aldrich	Cat # 702587
cOmplete protease inhibitor	Roche	Cat # 37378900
Unstained Protein Standard	Thermo Fisher Scientific	Cat # LC0725
DMEM without pyruvate	Wisent Bioproducts	Cat# 319-015
FBS	Wisent Bioproducts	Cat# 091-150
FBS	Gibco	Cat# 12483020
Micrococcal nuclease	Thermo Scientific	Cat# 88216
JumpStart™ Tag DNA Polymerase	Sigma-Aldrich	Cat #D9307
TRIzol™ Reagent	Thermo Fisher Scientific	Cat #15596026
Hygromycin B	Wisent Bioproducts	Cat # 450-141-XL
G418 sulfate	Wisent Bioproducts	Cat# 400-130-UG
Puromycin	Wisent Bioproducts	Cat # 400-160-EM
hexamethrine bromide (Polybrene)	Sigma-Aldrich	Cat # 107689
Sodium butyrate	Thermo Scientific Chemicals	Cat# AAA1107906
DMEM with L-glutamine & phenol red,without D-glucose	Wisent Bioproducts	Cat # 319-061-CL.
Dithiothreitol (DTT)	Inalco	Cat #1758-9030
4-20% native Polyacrylamide Gel	Bio-Rad	Cat # 4568094
Bovine Serum Albumin	BioShop	Cat # ALB001
ABT-263 (Navitoclax)	APExBIO	Cat # AA3007
ACRYLAMIDE/BIS-ACRYLAMIDE, 30% Solution, 37.5:1	Bioshop	Cat# ACR010.502
Deposited data		
RNAseq	This study	GSE220545
ATAC-seq	This study	GSE254358
Experimental models: Cell lines		
Phoenix Ampho packaging cells	S. W Lowe MSKCC, New York)	RRID:CVCL_H716
IMR90 (normal human diploid fibroblasts)	Coriell Institute for Medical Research (Camden, NJ).	Coriell Cat# I90-83, RRID:CVCL_0347
MRC5	Francis Rodier (CR-CHUM, Montreal)	RRID:CVCL_0440
HEK293T (embryonic kidney)	American Type Culture Collection (ATCC, Manassas, VA)	ATCC Cat# CRL-3216, RRID:CVCL_0063)

(*Continued on next page*)

Continued

REAGENT or RESOURCE	SOURCE	IDENTIFIER
KP4	Nabeel Bardeesy and Massachusetts General Hospital Center for Molecular Therapeutics (CMT)	RRID:CVCL_1338
Oligonucleotides		
Table S1 for qPCR primers, shRNA target sequences and PCR cloning primers.	This study	N/A
Recombinant DNA		
pBABE with selection marker puromycin, hygromycin or *neomycin*	Ferbeyre Laboratory	(Lessard et al.)[35]
pBABEpuromycin-H-RASV12	Ferbeyre Laboratory	(Lessard et al.)[35]
pBABE ER and pBABE-ER-RAS	Ferbeyre Laboratory	(Lessard et al.)[35]
pLXSN, pLXSN-E6, pLXSN-E7, pLXSN-E6/E7	Ferbeyre Laboratory	(Lessard et al.)[35]
MLPXneo and derivatives with shRNAs for NTC, ETV4, RUNX1, OCT1A, MAFB, ERK2	This study	N/A
MSCV Hygro and derivatives expressing ETV4, RUNX1, OCT1A, MAFB, cJUN, cFOS, GATA1, EHF, THRB	This study	N/A
Software and algorithms		
Prism 6-9	https://www.graphpad.com/	RRID: SCR_002798
Black Zen software	http://stmichaelshospitalresearch.ca/wp-content/uploads/2015/09/ZEN-Black-Quick-Guide.pdf	RRID:SCR_018163
ImageJ	https://imagej.net	RRID:SCR_003070
Aperio ImageScope	https://www.leicabiosystems.com/digital-pathology/manage/aperio-imagescope/	RRID:SCR_020993
FlowJo	https://www.flowjo.com/solutions/flowjo	RRID:SCR_008520
LightCycler Software	http://www.roche-applied-science.com/shop/products/absolute-quantification-with-the-lightcycler-carousel-based-system	RRID:SCR_012155
Bio-Rad CFX384 Real-Time Detection System	https://www.bio-rad.com/en-us/product/cfx384-touch-real-time-pcr-detection-system?ID=LJB22YE8Z	RRID:SCR_018057
FASTQC	http://www.bioinformatics.babraham.ac.uk/projects/fastqc/	RRID:SCR_014583
TRIMMOMATIC	http://www.usadellab.org/cms/index.php?page=trimmomatic	RRID:SCR_011848
BOWTIE2	http://bowtie-bio.sourceforge.net/bowtie2/index.shtml	RRID:SCR_016368
Samtools	http://htslib.org/	RRID:SCR_002105
deepTools	https://deeptools.readthedocs.io/en/develop/	RRID:SCR_016366
MACS2	https://github.com/macs3-project/MACS	RRID:SCR_013291
Diffbind	http://bioconductor.org/packages/release/bioc/html/DiffBind.html	RRID:SCR_012918
DESeq2	https://bioconductor.org/packages/release/bioc/html/DESeq2.html	RRID:SCR_015687
HOMER	http://homer.ucsd.edu/	RRID:SCR_010881
g:Profiler	http://biit.cs.ut.ee/gprofiler/	RRID:SCR_006809
GenomicRanges	http://www.bioconductor.org/packages/2.13/bioc/html/GenomicRanges.html	RRID:SCR_000025
STAR	http://code.google.com/p/rna-star/	RRID:SCR_004463
RSEM	http://deweylab.biostat.wisc.edu/rsem/	RRID:SCR_000262
GSEA	http://www.broadinstitute.org/gsea/	RRID:SCR_003199
DIRE	http://dire.dcode.org	RRID:SCR_003058

RESOURCE AVAILABILITY

Lead contact

Further information and requests for resources and reagents should be directed to and will be fulfilled by the lead contact, Gerardo Ferbeyre (g.ferbeyre@umontreal.ca).

Materials availability

All reagents generated in this study are available upon reasonable request to the lead contact.

Data and code availability

- The ATAC-seq data is available at GEO: GSE254358. RNAseq data is available at GEO: GSE220545.
- This paper does not report original code.
- Any additional information required to reanalyze the data reported in this paper is available from the lead contact upon request.

EXPERIMENTAL MODEL AND SUBJECT PARTICIPANT DETAILS

Cells

Phoenix-Ampho packaging cells were a gift from S. W Lowe. HEK-293T cells were obtained from American Type Culture Collection (ATCC, Manassas, VA). KP4 was a gift from N. Bardeesy. IMR90 was obtained from the Coriell Institute for Medical Research (Camden, NJ). MRC5 was a gift from F. Rodier. All cell lines were cultured in Dulbecco's modified Eagle medium (DMEM #319-015-CL; Wisent) and supplemented with 10% FBS (FBS, Cat. no. 12483020 Gibco for Phoenix, HEK293T and KP4; or FBS Premium, Cat. no. 091–150 Wisent for IMR90 and MRC5), 1% penicillin/streptomycin sulfate (Cat. no. 450-201-EL, Wisent) and 2 mM L-glutamine (Cat. no. 609-065-EL, Wisent).

Plasmids

Retroviruses pBABE, pBABE-H-RasV12, pBABE-ER, pBABE-ER-RAS, pLXSN, pLXSN-E6, pLXSN-E7, pLXSN-E6/E7 were described previously.[35] MLPXneo backbone used to clone the following shRNAs (NTC, ETV4, RUNX1, OCT1A, MAFB, ERK2) was generated by subcloning the *Neo*/Kan resistance cassette from MSCVneo into MLPpuro with shRNAs using AgeI/ClaI restrictions sites. These shRNAs were cloned according to[67] and using XhoI/EcoRI restriction sites. Plasmids for overexpression of TFs were either PCR cloned from cDNA originating from IMR90 ER-RAS at Day3 of 4OHT treatment using: BamHI/NotI for MAFB (NM_005461), NotI/XhoI for EHF (NM_012153), BamHI/XhoI for cFOS (NM_005252), NotI/XhoI for THRB (NM_000461) and XhoI/HpaI for OCT1A (NM_002697), or PCR cloned from vectors acquired from Addgene: RUNX1 was subcloned from Addgene's EF1a_RUNX1_P2A_Hygro_Barcode (Plasmid #120475) into BsaA1/NotI restrictions sites, ETV4 was subcloned from Addgene's ETV4_pet28a (Plasmid #131645) into BamHI/NotI restrictions sites, cJUN was subcloned from Addgene's pMIEG3-*c*-Jun (Plasmid #40348) into BamHI/XhoI restrictions sites and finally, GATA1 was subcloned from Addgene's hGATA-1 WT (Plasmid #118352) into NotI/XhoI restrictions sites. In all cases, the digested PCR was introduced into the pre-digested MSCVhygro backbone. For PCR primers used for cloning see Table S1.

METHOD DETAILS

Viral transduction of cells

Retroviral or lentiviral mediated gene transfer was done according to,[3] but doing only one round of infection with either half a viral soup or a quarter of a viral soup. The viral soups were then filtered with a 0.45 μm filter, supplemented with 4 μg/mL of polybrene (Sigma), and added to target cells. Twenty-four hours after infection, media was changed and 30 h after infections, cells were selected using the following Wisent-purchased antibiotics: puromycin dihydrochloride (1.25 μg/mL in IMR90/MRC5 and 2.18 μg/mL in KP4) and/or hygromycin (37.5 μg/mL in IMR90/MRC5 and 250 μg/mL in KP4) and/or G418 (500 μg/mL in IMR90/MRC5).

Chromatin fractionation

Chromatin-bound proteins were obtained using the protocol in.[68] For each condition in IMR90 cells, 2 × 10cm plates at 80% confluency were used. Briefly, cells were washed once in PBS and then harvested by scraping in 1mL of ice-cold PBS. Cells were next spined down at 130 x g for 3 min at 4°C and supernatant was discarded. The cell pellet was resuspended by pipetting up and down 5 times with 5 volumes of ice-cold E1 buffer (50 mM HEPES-KOH pH 7.5, 140 mM NaCl, 1 mM EDTA pH 8.0, 10% glycerol, 0.5% NP-40, 0.25% Triton X-100, 1 mM DTT and 1x protease inhibitor cocktail) per 1 volume of cell pellet. Cells were spined down at 1100 x g for 2 min at 4°C and supernatant (cytoplasmic fraction) was transferred into a separate tube. The cell pellet was resuspended once again in the same volume of E1 buffer and spun down at 1100 x g for 2 min at 4°C. The supernatant was discarded, and the pellet was resuspended for the last time in the same volume of E1 buffer before a 10-min incubation on ice. Cells were once again spined down at 1100 x g for 2 min at 4°C and the supernatant was discarded. The pellet was resuspended in 2 volumes of ice-cold E2 buffer (10 mM

Tris-HCl pH 8.0, 200 mM NaCl, 1 mM EDTA pH 8.0, 0.5 mM EGTA pH 8.0, and 1x protease inhibitor cocktail). Cells were spined down at 1100 x g for 2 min at 4°C and the supernatant (nucleoplasmic fraction) was transferred into a separate tube. As with the E1 buffer, the cell pellet was washed once again with 2 volumes of E2 buffer, spun down, and then re-incubated a last time for 10 min on ice with the E2 buffer before centrifugation at 1100 x g for 2 min at 4°C. The supernatant was discarded once again. The pellet (chromatin fraction) was carefully resuspended with 5 volumes of ice-cold E3 buffer (500 mM Tris-HCl pH 8.0, 500 mM NaCl, and 1x protease inhibitor cocktail) per cell pellet volume (enough for a sonication probe), making sure not to lose the pellet as it is sticky. Extracts were sonicated for 5 min, 15 s ON/15 s OFF at 20% of maximum power using an FB120 sonicator (Fisher Scientific) with a CL-18 probe. All cellular fractions for each condition were next spined down at 16,000 x g for 10 min at 4°C and the supernatant was transferred into new tubes. Protein concentration was assessed using Pierce BCA Protein Assay kit and plates were read with a spectrophotometer at 562nm.

Western-blots

Western blots were performed as previously described.[35] For antibodies see Table S2.

MNase assays

For each condition, 2-10x10^6 cells (for IMR90: 1 × 10cm plate at ±90% confluency with or without hyperproliferation) were pelleted at 500 x g for 5 min at room temperature. It is important to know the exact number of cells at this step, to adjust the quantity of enzyme later to ensure the same ratio of enzyme units per cell between each condition for this assay. Cells were then washed once in PBS and pelleted once again at 500 x g for 5 min at room temperature. For each condition, cells were crosslinked by resuspending the cell pellet in 10mL of 1% formaldehyde in PBS and tumbled end over end for 10 min at room temperature. The crosslinking reaction was stopped by adding 30mL of 1M Tris-HCl pH 8.0 to a final concentration of 750mM agitating by tumbling for 2 min at room temperature. Cells were next pelleted at 750 x g for 5 min at room temperature, resuspended in PBS to wash, and re-pelleted once again at 750 x g for 5 min at room temperature. Cells were next resuspended in 1mL PBS and transferred in an Eppendorf before centrifugating at 750 x g for 5 min. The supernatant was then discarded before flash-freezing the cell pellet in liquid nitrogen. Pellets were kept at −80°C until ready to proceed further. For MNase digestion, the cell pellet was resuspended in PBS +0.1% Triton X-100 + 1mM $CaCl_2$ to get 1x10^6 cells per 200μL and incubated for 2 min at room temperature. Then, 0.5U of Micrococcal nuclease (Cat. no.88216, Thermo Scientific) per million cells was added to the resuspended cells and the digestion tube was incubated at 37°C. After 5 min, 200μL of the digestion tube was transferred to new Eppendorf tubes containing final concentrations of 10mM EDTA and 5mM EGTA, and these tubes were kept on ice while processing the next conditions to halt the reaction. The samples were then adjusted to 0.5% SDS and 10 mM Tris-HCl pH 8.0. Samples were then incubated with RNase 1X (Roche) for 30 min at 37 °C, then with 400 μg/mL of Proteinase K (NEB) for 120 min at 55 °C, and then incubated at 65 °C for 60 min to reverse crosslinks. DNA was then recovered by phenol-chloroform extraction followed by ethanol/sodium acetate precipitation. Briefly, one volume of phenol:chloroform: isoamyl alcohol (Sigma) was added to each sample and the tubes were inverted thoroughly by hand for ±20 s. Samples were centrifuged for 5 min at 16,000 × g at room temperature. The upper phase was carefully pipetted and transferred to a fresh tube. Then, 0.1 volume of 3M Sodium Acetate pH 5, 2 volumes of 100% Ethanol, and 10μg of glycogen (ThermoFisher Scientific, Cat.no. R0551) were added to each tube and quickly vortexed. Samples were chilled at −20°C for 30 min and then spined at 4 °C at 16,000 x g for 10 min. The supernatant was discarded, and the pellet was washed with 750μL of cold 70% EtOH before centrifugation at 4 °C at 16,000 x g for 5 min. The supernatant was again discarded, and the pellet was air dried for ±10 min before dissolving it with a 1 mM Tris-HCl pH 8.0 and 0.1 mM EDTA solution. Samples were resolved on a 1.5% agarose gel and visualized with ImageJ software to quantify mononucleosomes (band at ±146 bp), heterochromatin (>1500bp smear), and total DNA intensity for each lane. The percentage of net chromatin opening was obtained by normalizing the intensity (I) of the mononucleosome band on the heterochromatin band for each lane.

$$\%\ net\ chromatin\ opening = \frac{Opening}{Closure} = \frac{\frac{I_{mono}}{I_{total}} \times \frac{1}{U_{enz}/I_{tot}}}{\frac{I_{1.5kb+}}{I_{total}} \times \frac{1}{U_{enz}/I_{tot}}} = \frac{I_{mono}/U_{enz}}{I_{1.5kb+}/U_{enz}} = \frac{I_{mono}}{I_{1.5kb+}}$$

Cell proliferation assay

Proliferation and colony assay (assessed by a crystal violet retention assay) were performed as previously described.[35] Briefly, cells (10,000–15,000 cells for IMR90/MRC5 and 20,000 cells for KP4) were plated in several 12-well plates with 3 technical replicates for each biological replicate. One plate of each condition and time point was fixed by a 10-min incubation at room temperature with a 1% glutaraldehyde solution in PBS 1X and then washed in PBS. During growth assays, media was replaced every 2–3 days. After fixation of all time points, cells were stained with 0.1% crystal violet in PBS for 30 min at room temperature under agitation. The crystal violet solution was then removed and plates were washed in tap water 15 times until no more crystal violet could dissolve in water. Plates were then dried at room temperature for at least 24h. To assess growth, crystal violet was dissolved in 10% acetic acid in water for 20 min under agitation. An equal volume of dissolved crystal violet solution was then transferred in 96-well plates and OD was

measured at 590nm. To avoid saturation of dissolved crystal violet, twice or thrice the volume of 10% acetic acid was used for very confluent wells; and OD values were multiplied with dilution factor. OD values were finally normalized on values at Day 0 for each condition, before normalizing on experimental internal control.

SA-β-gal assay

For IMR90 and MRC5, cells were washed with PBS and then fixed in 0.5% glutaraldehyde in PBS for 15 min at room temperature 4–5 days after plating. Cells were then rinsed twice with PBS and incubated twice for 10 min in PBS at pH 6.0 with 1mM $MgCl_2$. This solution was then replaced by the pre-warmed and pre-filtered (0.45μm) staining solution (PBS pH 6.0, 1mM $MgCl_2$, 1 mg/mL X-Gal, 5mM potassium ferricyanide and 5mM potassium ferrocyanide) and cells were incubated for 1–6 h at 37°C protected from the light. For KP4, we used the same protocol except for the staining solution which is prepared in Milli-Q water rather than PBS and contains 40mM citric acid, 40mM Sodium Phosphate Monobasic pH 6.0, 150mM NaCl, 200mM $MgCl_2$, 1 mg/mL X-Gal, 5mM potassium ferricyanide and 5mM potassium ferrocyanide. For all SA-β-gal assays, reactions were stopped by replacing the staining solution with 100mM Tris-HCl pH 8.0. Pictures were taken with an Evos XL Core light microscope (AMEX1000 from Invitrogen).

Histology and immunohistochemistry

Normal and neoplastic pancreatic tissues were obtained from the CHUM Hepatopancreatobiliary Cancer Biobank and Database, approved by the institutional review board (No. 09.237), from patients who provided written informed consent. Identification of tissues and areas with normal, low-grade dysplasia, high-grade dysplasia, well and poorly differentiated pancreatic ductal adenocarcinoma was done by pathologists (F.A., V.Q.-H.T.) on H&E-stained tissue slides. Selected tissue blocks were cut into 4μm slides. After normal deparaffinization, tissues were stained using the Benchmark XT automated stainer (Ventana Medical Systems, Roche). Antigen retrieval was then performed using Tris-EDTA buffer, pH 7.8 (Cell Conditioning #1 solution from Ventana Medical System Inc.) for 60 min at 95°C. Slides were then incubated at 37°C with anti-ETV4 antibody (1:350, PA5-99226, Invitrogen) or anti-RUNX1 antibody (1:250, ab23980, Abcam) for 60 min. Revelation was performed using the DAB Detection Kit (Ventana Medical System Inc.). Finally, tissue sections were counterstained with hematoxylin and bluing reagent (Ventana Medical System Inc.). Slides were scanned using the Aperio Verso 200 slide scanner microscope with a 20 × 0.8 NA objective with a 0.275MPP resolution (Leica Biosystems). Scoring of IHC staining was performed by two pathologists, among which a GI specialist, using the Image Scope software (Leica Biosystems) for visualization of slides.

Immunofluorescence and FACS analysis

Immunofluorescence experiments were done according to.[3] For antibodies, see Table S2. Images were acquired with a Zeiss Axio Imager Z2 upright microscope using 63X or 100X objectives with a sCMOS 16-bit Prime camera (Photometrics) and/or CCD 12-bit AxioCam MRm3 camera (Zeiss) and ZEN 2 Imager (2.0.14283.302). Images were processed with the ZEN Black Software.

For FACS, cells were first trypsinized and washed with PBS. Then, for each condition, 500,000 cells were resuspended and incubated with 0.5mL of 4% PFA for 10 min at 37°C. These cells were then washed with PBS-BSA 2%, followed by permeabilization with 1mL of cold 90% methanol (MeOH) drop by drop under the vortex. Cells were then kept in MeOH for 30 min in ice. Subsequently, 3mL of PBS-BSA 2% was added to each tube for washing. Cells were then resuspended in 1mL of PBS-BSA 2% and split into two tubes, each containing 250,000 cells in 0.5mL. Cells were once again washed by completing each tube with an additional 3mL PBS-BSA 2%. Cell pellets were then resuspended in 50μL of PBS-BSA 2% with primary antibody and incubated at room temperature for 1h. Of note, the same amount of antibody (in ng) was used for rabbit IgG control isotype (Cell Signaling, 3900S) and *p*-ERK antibody (Cell Signaling, 4370). Cells were then washed again with PBS-BSA 2% and the pellet was resuspended in 50μL of the same solution but with the secondary antibody this time (Alexa Fluor 647 goat anti-rabbit IgG Invitrogen). Cells were incubated for 30 min at room temperature in the dark and then washed with PBS-BSA 2%. Cells were finally resuspended in 250μL of PBS and analyzed by flow cytometry with the BD FACSymphony A3 Cell Analyzer.

RT-qPCR

Total RNA was extracted from samples using TRIzol (Invitrogen) according to the manufacturer's instructions and then reverse transcribed using All-In-One 5X RT MasterMix (ABM, Cat.no. G592). Gene expression was determined with a LightCycler 96 (software version 1.1) Real-Time PCR System (Roche Applied Science) or with a CFX384 (software CFX Maestro version 1.1) Real-Time system (Bio-Rad), using SYBR Green technologies as described previously.[69] Used qPCR primers are presented in Table S1.

ATAC-seq

Cells were harvested, and counted, and then 100K cells were resuspended in 500μL of Freezing medium (50% FBS/40% growth media/10% DMSO) and kept in a liquid nitrogen tank until shipping. These cells were then shipped to Active Motif for preparing ATAC-seq libraries and sequencing (cat. no.53150). The quality of the raw reads was assessed with FASTQC v0.11.9. After examining the quality of the raw reads, trimming was performed with TRIMMOMATIC v0.36. The reads were aligned to the human reference genome (release v104) with BOWTIE2 v2.3.5 with a mean of 99% of reads uniquely mapped. Alignments were post-processed to remove PCR duplicates (Picard tool v2.26.3) and reads mapping to mitochondrial DNA (Samtools v1.10). To represent the real Tn5

transposase binding sites of 9bp, the coordinates of the reads were shifted by +4bp for the plus strand and by -5bp for the minus strand, using deepTools v3.5.1. The former was also used to remove ENCODE's blacklisted regions (signal artifacts regions) and convert bam files to BEDPE format. MACS2 was used to identify significant peaks. Diffbind v3.10.0 R (v4.3.1) package was used to generate the count matrix of Tn5 insertion site numbers for each consensus peak (peaks that were present in all samples). Differentially accessible regions (DARs) were identified between conditions using DESeq2 v1.40.2 R (v4.3.1) package.

DARs were annotated with their closest feature and different transcription binding motifs identified with HOMER v4.11. A non-biased motif search was also performed with HOMER v4.11, to identify all known motifs and *de novo* motifs in these regions. In this step, the consensus peaks among all three conditions were considered as background. Some motifs were not very abundant in the target sequences, but they are still significant given that they were very rare in the background sequences.

For each comparison, statistically significant DARs (padj ≤ 0.05) were separated into 2 groups: more open and more closed, according to the sign of their log2 fold-change values. These groups were used for genome ontology distribution figures as well as gene ontology analyses with gProfiler v1.0.0. The closest annotated gene to each DAR was used for gene ontology enrichment. Results of gProfiler were only considered if the term size was between 15 and 2000, and an intersection size of at least 3. Heat maps were built by comparing DARs shared for the comparisons 12 vs. 1.5, 3 vs. 12, and 3 vs. 1.5 and called common DARs (Figure 3A) or by considering all open DARs unique for each condition (Figure S4B). Bioinformatics analyses were performed at the Bioinformatics core facility from Montreal Clinical Research Institute (IRCM).

NAD and LAD annotations were retrieved from Chan et al. 2022 supplementary materials (https://www.ncbi.nlm.nih.gov/pmc/articles/PMC8933007/). The intersection of all common peaks NADs or LADs was performed with bedtools v2.31.0, GenomicRanges" and "tracklayer". After reading DARs and genomic coordinates of LADs and NADs, GRanges object was generated using GenomicRanges package. FindOverlaps from the GenomicRanges package was used to find overlaps between the peaks and LADs/NAD. Then ggplot2 was used to create violin plots. These two plots are used for visualization of the distribution of log2FoldChange values for peaks overlapping with NADs and LADs. It includes peaks that are in NADs vs. not in NADs, and also the same for LADs. The genomic coordinates for repetitive sequences were downloaded from the UCSC Genome Browser, hg38 genome assembly.

RNA-seq: Library preparation for RNA-Sequencing and data analysis

RNA was extracted as above mentioned in the RT-qPCR section until the precipitation step. However, once at the RNA precipitation step, isopropanol-containing RNA samples were loaded on an RNeasy column (Qiagen Mini Kit #74106). RNA was obtained following the protocol in the kit and then solubilized in 50μL of RNAse-free water. RNA quality was assessed on a BioAnalyzer (RNA Nano for >100K cells) and concentration was determined using Qubit BR. All samples had a RIN above 9.5. Then, 1000 ng of total RNA was used for library preparation using the KAPA mRNAseq Hyperprep kit (KAPA, Cat no. KK8581). Ligation was made with 64 nM final concentration of Illumina index and 9 PCR cycles were required to amplify cDNA libraries. Libraries were quantified by QuBit and BioAnalyzer DNA1000. All libraries were diluted to 10 nM and normalized by qPCR using the KAPA library quantification kit (KAPA; Cat no. KK4973). Libraries were pooled to equimolar concentration. Sequencing was performed with the Illumina Nextseq500 using the Nextseq High Output Kit (86 cycles) using 2.2 p.m. of the pooled libraries. Around 20 M single-end PF reads were generated per sample. Library preparation and sequencing was made at the Institute for Research in Immunology and Cancer's Genomics Platform (IRIC).

Sequences were trimmed for sequencing adapters and low-quality 3′ bases using Trimmomatic version 0.35[70] and aligned to the reference human genome version GRCh38 (gene annotation from Gencode version 26, based on Ensembl 88) using STAR version 2.5.1b.[71] Gene expressions were then obtained both as read count directly from STAR as well as computed using RSEM[72] to obtain gene and transcript level expression, either in TPM or FPKM values, for these stranded RNA libraries. DESeq2 version 1.18.1[73] was then used to normalize gene read counts. GSEA was used to identify gene sets that are concordant with the transcript that changed upon commitment.[74] Transcription factors acting on differentially expressed genes were predicted using DIRE (https://dire.dcode.org/).

Analysis of the dynamics of commitment

To understand the transition through the SeRP, we mapped the expression of the senescent phenotype (S) as a function of the changes in RAS-MAPK signals induced by 4OHT over different days. The percent of senescence cells increases and saturates to a particular value which can be seen through a 3D Hill function fit i.e.,

$$S = \alpha \frac{x^n}{(K_1{}^n + x^n)} \frac{t^m}{(K_2{}^m + t^m)} \quad \text{(Equation 1)}$$

where, α is the maximum value for senescent cells induction, n and m are Hill's coefficients corresponding to RAS-MAPK signal intensity and time. The value of n is 4.57 and m is 7.06. Furthermore, we fit the equation using Python's *curve_fit* function in the raw dataset to estimate the parameters of this 3d Hill function as shown in Fig.1M-N.

QUANTIFICATION AND STATISTICAL ANALYSIS

Statistical analysis (two-tailed Student's t-test) was performed using GraphPad Prism 8 and One-way ANOVA with post-hoc Tukey HSD Test using the Astatsa website. A value of $p < 0.05$ was considered statistically significant. Experiments were repeated at least three times, with some exceptions indicated in figure legends. Experiments that were performed less than three times include three technical triplicates.